Collisional depolarization of NO(A) by He and Ar studied by quantum beat spectroscopy.

M. Brouard,* H. Chadwick, Y.-P. Chang, R. Cireasa,† C.J. Eyles, A.O. La Via, and N. Screen

The Department of Chemistry, University of Oxford,

The Physical and Theoretical Chemistry Laboratory,

South Parks Road, Oxford, OX1 3QZ, United Kingdom.

F. J. Aoiz‡

Departamento de Química Física, Facultad de Química,

Universidad Complutense, 28040 Madrid, Spain

J. Kłos§

Department of Chemistry and Biochemistry,

University of Maryland, College Park, MD, 20742, USA

(Dated: July 14, 2009)

Abstract

Zeeman and hyperfine quantum beat spectroscopies have been used to measure the total elastic plus inelastic angular momentum depolarization rate constants at 300 K for NO($A^2\Sigma^+$) in the presence of He and Ar. In the case of Zeeman quantum beats it is shown how the applied magnetic field can be used to allow measurement of depolarization rates for both angular momentum orientation and alignment. For the systems studied here, collisional loss of alignment is more efficient than loss of orientation. In the case of NO(A) with He, and to a lesser extent NO(A) with Ar, collisional depolarization is found to be a relatively minor process compared with rotational energy transfer, reflecting the very weak long range forces in these systems. Detailed comparisons are made with quantum mechanical and quasiclassical trajectory calculations performed on recently developed potential energy surfaces. For both systems, the agreement between the calculated depolarization cross-sections and the present measurements is found to be very good, suggesting that it is reasonable to consider the NO(A) bond as frozen during these angular momentum transferring collisions. A combination of kinematic effects and differences in the potential energy surfaces are shown to be responsible for the differences observed in depolarization cross-section with He and Ar as a collider.

*Electronic address: mark.brouard@chem.ox.ac.uk

†Current address: Laboratoire Collisions Agrégats Réactivité, Université Paul Sabatier, Bât. 3R1b4, 118 route de Narbonne 31062, Toulouse, Cedex 09, France

‡Electronic address: aoiz@quim.ucm.es

§Electronic address: jklos@umd.edu

I. INTRODUCTION

Angular momentum polarization effects are ubiquitous in chemistry [1, 2]. Collisional processes can generate polarized reaction products, and may proceed with different rates depending on the polarization state of the reactants [3–5]. The study of the product rotational angular momentum polarization in molecular photodissociation and bimolecular reactions provides detailed insight into the reaction mechanism, in particular yielding information about the bending and torsional forces in operation as the reaction proceeds [3, 4, 6–11]. In the present work, as well as in our previous related studies [12–16], we show how the collisional depolarization of molecules provides detailed insight about the dynamics of inelastic, rotational energy transfer (RET) collisions [17]. Angular momentum polarization is also central to all photon-induced processes, including photoionization and photodissociation, due to the inherent anisotropic nature of the absorption and emission of light [1, 6–8]. Knowledge of angular momentum polarization is of practical importance in the quantitative interpretation of atomic and molecular spectra [18], and it is also relevant to bulk properties such as molecular gas flow [19]. There has been considerable recent interest in the polarization of electronic angular momentum, principally in the atomic products of molecular photodissociation [20–24]. The motivation for these studies lies in the fact that the electronic angular momentum polarization provides a direct probe of the motion of the electrons during photofragmentation or reaction [25]. Finally, angular momentum polarization is important in magnetic resonance techniques such as nuclear magnetic and electron spin resonance [2].

In the present work we apply the techniques of Zeeman and hyperfine quantum beat spectroscopy to the measurement of angular momentum polarization effects [13–16, 26]. One advantage of this method is that it provides the polarization information on a shot-by-shot basis, in some cases reducing the need for multiple pump-probe polarization geometries and data subtraction. In fact, analogous to magnetic resonance techniques, for alignment measurements the polarization information can be obtained directly from the Fourier transform of the laser induced fluorescence (free induction) decay. Here we show for the first time how it is possible to use Zeeman quantum beat spectroscopy to measure collisional depolarization of angular momentum orientation, as well as alignment. Such orientation measurements could not be made easily using conventional laser induced fluorescence (LIF)

techniques, since they require pointing the laser probe radiation directly towards the fluorescence detector [16]. The role of the weak magnetic field is thus to rotate the orientation generated by the probe laser onto the fluorescence detection axis.

Here we follow our previous studies of collisional depolarization of OH(A) [12–15] by applying the quantum beat technique to the collisional depolarization of NO(A) by He and Ar. Both NO(A) and OH(A) are $^2\Sigma^+$ radicals, and collisions with the rare gases lend themselves to a common theoretical treatment. We have recently shown in the case of OH(A) + Ar that electron and nuclear spin can be treated as spectators to the dynamics to a very good approximation [12, 15]. In the spectator limit, because the directions of the electron and nuclear spin are unchanged by collision, the cross-sections for spin-rotation and hyperfine level changing collisions are purely determined by the extent to which the rotational angular momentum is reoriented during collision, since this reorientation leads to a recoupling of the spin and rotational angular momenta [27–30]. Once the angular distribution between $\boldsymbol{j}$ and $\boldsymbol{j}'$ has been determined classically, then simple angular momentum recoupling formulae can be used to determine reliably the cross-sections for spin-rotation and hyperfine changing collisions [14, 15]. Based on the relative magnitudes of the spin-rotation coupling constants of OH(A) and NO(A) [31, 32], it seems reasonable to suppose that the electron spin in NO(A) + Ar/He collisions will also be well approximated as a spectator, and the same theoretical treatment to that presented previously for OH(A) + Ar [15] should be applicable.

The outline of the paper is as follows. Section II describes the experimental and theoretical procedures employed, and the methods used to analyze the Zeeman and hyperfine quantum beats. In Section III we present the NO($A^2\Sigma^+$) state-specific angular momentum depolarization rate coefficients and velocity averaged cross-sections. Particular attention is also paid to the quantitative simulation of the time-dependent beat amplitudes using the results of quasi-classical trajectory (QCT) calculations. Exact quantum mechanical (QM) scattering calculations are used to confirm the reliability of the QCT calculations. Section IV provides a detailed comparison with previous experimental and theoretical work. The final section summarizes our principal conclusions.

II. METHOD

A. Calculation details

1. Notation

As previously [12, 14, 15] we employ the following notation. $\boldsymbol{N}$ ($\boldsymbol{N'}$) denotes the initial (final) state diatomic rotational angular momentum apart from electron and nuclear spin. For a diatomic radical in a $^2\Sigma^+$ electronic state, for which electronic orbital angular momentum is zero, $\boldsymbol{N}$ ($\boldsymbol{N'}$) is equivalent to the nuclear rotational angular momentum, which must lie perpendicular to the internuclear axis, $\boldsymbol{r}$. The corresponding quantum number is written N (N'). The total rotational angular momentum apart from nuclear spin of NO($A^2\Sigma^+$) is denoted by $\boldsymbol{j}$, and its quantum number as j. Note that in cases in which NO(A) is treated as a closed shell species, $N = j$. In the Hund's case (b) coupling scheme appropriate for NO(A), the molecular wavefunction is defined by $\boldsymbol{j} = \boldsymbol{N} + \boldsymbol{S}$, where $\boldsymbol{S}$ is the electronic spin. The reactant and product quantum numbers F and F' are associated with the total diatomic angular momentum, including both electron and nuclear spin, *i.e.* $\boldsymbol{F} = \boldsymbol{j} + \boldsymbol{I}$. The total angular momentum quantum number of the collision system (*i.e.* NO(A) + Ar/He in the application discussed in Sections II and III) is denoted by J and its projection onto the space fixed Z axis by M_J.

2. General theory

The quantities measured in the present experiments are collisional depolarization rate constants, which can be converted into velocity averaged cross-sections (see below). These depolarization cross-sections can be thought of as measures of the $\boldsymbol{j}$-$\boldsymbol{j'}$ vector correlation [5, 15, 27, 33], which quantifies the tilt of the angular momentum subsequent to a collision. In both the classical and quantal descriptions of collisional depolarization it is possible to relate the polarization moments *after* a collision, $\mathcal{P}_q^{(k)}(j')$, to the *extrinsic* moments of the initial state, $r_q^{(k)}(j)$, by [15, 27, 33]

$$\mathcal{P}_q^{(k)}(j') = a^{(k)}(j, j')\, r_q^{(k)}(j)\,. \tag{1}$$

This equation is valid provided neither the initial nor the final directions of motion are defined. Classically, it is readily shown that the depolarization moments (or multipole transfer coefficients), $a^{(k)}(j,j')$, are directly related to the $\boldsymbol{j}$-$\boldsymbol{j}'$ vector correlation by the expression [15]

$$P(\theta_{jj'}) = \frac{1}{2}\sum_k [k]\ a^{(k)}(j,j') P_k(\cos\theta_{jj'})\ , \tag{2}$$

where $[k] = (2k+1)$, $P_k(\cos\theta_{jj'})$ is the $k^{\rm th}$ Legendre polynomial, and the depolarization moments are defined as

$$a^{(k)}(j,j') = \langle P_k(\cos\theta_{jj'})\rangle\ . \tag{3}$$

The quantum mechanical calculation of the depolarization moments has been discussed in detail in a number of papers [15, 27, 34–36]. When the initial and final directions of motion are unresolved, the multipole transfer coefficients are defined [5, 15, 27, 33–39]

$$a^{(k)}(j,j') = [k]\,\frac{S^{(kk)}_{qq}(j,j')^\star}{S^{(00)}_{00}(j,j')} = \frac{\sigma^{(kk)}(j,j')}{\sigma^{(00)}(j,j')}\,, \tag{4}$$

where $\sigma^{(kk)}(j,j')$ appearing in Eq. 4 are the tensor cross-sections of Follmeg *et al.* [33–35], while $S^{(kk)}_{qq}(j,j')^\star$ are the *correlation coefficients* $S^{(kk)}_{qq}(j,j')^\star$ defined by Miranda and coworkers [37–39]. Expressions relating these coefficients to the scattering $\boldsymbol{T}$-matrix elements have been presented by a number of authors [5, 27, 33].

We have shown previously that at fixed relative velocity, $v_{\rm r}$, the bimolecular rate constants for collisional depolarization are given by [14]:

$$k^{(k)}_{j\to j'} = k_{j\to j'}\ \left[1 - a^{(k)}(j,j')\right] = v_{\rm r}\,\sigma_{j\to j'}(v_{\rm r})\ \left[1 - a^{(k)}(j,j')\right]\ , \tag{5}$$

where $k_{j\to j'}$ and $\sigma_{j\to j'}(v_{\rm r})$ are the collision rate constants and cross-sections, respectively. Note that the depolarization rate constants and cross-sections are related by $k^{(k)}_{j\to j'} = v_{\rm r}\sigma^{(k)}_{j\to j'}$. The quantum mechanical derivation of this expression has been presented recently by Dagdigian and Alexander [34–36]. Note that in terms of the tensor cross-sections of Eq. 4 we can write the depolarization cross-sections [34–36]

$$\sigma^{(k)}_{j\to j'} = \sigma_{j\to j'}(v_{\rm r})\ \left[1 - a^{(k)}(j,j')\right] = ([j']/[j])^{1/2}\left[\sigma^{(00)}(j,j') - \sigma^{(kk)}(j,j')\right]\ . \tag{6}$$

If the total collision rate constants are known, the measurement of the depolarization rate constants therefore allows direct evaluation to be made of the $\boldsymbol{j}$-$\boldsymbol{j}'$ vector correlation, as quantified by the $a^{(k)}(j,j')$ expansion coefficients. From the classical definition

of the polarization parameters, Eq. (3), it is clear that $a^{(2)}(j,j')$ must lie within the limits $-\frac{1}{2} \leq a^{(2)}(j,j') \leq 1$, and consequently the alignment depolarization rate constant is bounded by $1\frac{1}{2}k_{j\to j'} \geq k^{(2)}_{j\to j'} \geq 0$. Therefore, when $a^{(2)}(j,j')$ is negative, the depolarization rate constant can exceed the collision rate constant. Similarly, since $a^{(1)}(j,j')$ ranges from $-1 \leq a^{(1)}(j,j') \leq 1$, the orientation depolarization rate constant must lie between $2k_{j\to j'} \geq k^{(1)}_{j\to j'} \geq 0$. These equations provide a convenient link between the measured depolarization rates constants, and the dynamically interesting ***j*-*j′*** depolarization parameters, $a^{(k)}(j,j')$. The limits on the quantum mechanical $a^{(k)}(j,j')$ parameters can differ from the values given above at low N, as has been discussed in general terms previously [15, 40].

The depolarization rate constants, cross-sections, and depolarization parameters obtained in the present work are averaged over a number of elastic and inelastic scattering processes, as described previously [14] (see also Section III C 2). The present experiments are conducted under thermal conditions, and hence the measured quantities are also averages over a 300 K Maxwell-Boltzmann distribution of relative velocities. The velocity averaged value of $a^{(k)}(j,j')$ can then be written [14]:

$$\langle a^{(k)}(j,j')\rangle = \frac{\langle v_{\rm r}\, \sigma_{j\to j'}(v_{\rm r})\, a^{(k)}(j,j';v_{\rm r})\rangle}{\langle v_{\rm r}\, \sigma_{j\to j'}(v_{\rm rel})\rangle}\,, \tag{7}$$

such that

$$\langle k^{(k)}_{j\to j'}\rangle = \langle k_{j\to j'}\rangle \, \left[1 - \langle a^{(k)}(j,j')\rangle\right] \,. \tag{8}$$

Finally, we can define the total depolarization rate constant for a specific initial state j as [14]

$$k^{(k)}_j(T) \equiv \langle k^{(k)}_j\rangle = \sum_{j'} \langle k_{j\to j'}\rangle \, \left[1 - \langle a^{(k)}(j,j')\rangle\right] \,. \tag{9}$$

A similar expression can be written for the final state averaged collision and depolarization cross-sections, $\langle \sigma^{(k)}_j\rangle$. The present article focusses specifically on the depolarization cross-sections with $k = 1$ and $k = 2$.

3. QM Method

Fully quantum close-coupling (CC) scattering calculations were performed using the new, rescaled *ab initio* potential energy surfaces (PESs) of Kłos *et al.* [41]. As in our previous work [12, 14, 15], the open shell (o–s) electronic structure of the NO(A) molecule was

taken into account in the QM scattering calculations using the HIBRIDON suite of codes [42], which employs a hybrid propagator comprised of the Log-Derivative propagator by Manolopoulos [43, 44] and the Airy propagator for the long-range region. For the closed shell (c–s) calculations of the integral cross-sections we employed the MOLSCAT code [45] with the same propagator.

In the CC scattering calculations of the closed shell NO(A) + Ar and NO(A) + He systems, the propagation was performed from 5 bohr to 60 bohr. The rotational basis of NO(A) ranged up to $N = 16$ for total energies up to $330\,\mathrm{cm}^{-1}$, and $N = 19$ for total energies up to $730\,\mathrm{cm}^{-1}$. In the log-derivative integration 25 radial steps were used. The total angular momentum was set automatically in MOLSCAT to converge the cross-sections. For the highest total energies it was necessary to include partial waves up to $J = 220$ for NO(A) + Ar and $J = 130$ for NO(A) + He. The o–s CC QM scattering calculations were performed with similar convergence and basis parameters as in the case of the c–s calculations.

The quantum mechanical polarization parameters were obtained from the tensor cross-section [33–36] output of Hibridon [42], using the definitions in ref. [15].

4. QCT Method

The QCT procedure employed to calculate the depolarization cross-sections follows that recently described in detail and applied to OH(A) + Ar [15], and will only be described briefly here. Batches of approximately 1×10^5 trajectories were run for several initial N states at a fixed collision energy of 39 meV for He + NO(A) and Ar + NO(A). This collision energy corresponds to the mean of a thermal distribution at 300 K ($\langle E_{\mathrm{coll}} \rangle = \frac{3}{2} k_{\mathrm{B}} T$). Since the PES for NO(A) + Ar and NO(A) + He have only been calculated for NO(A) at its equilibrium internuclear distance [12], the method of Lagrange multipliers was used to force rigid rotor behavior during the integration of the classical equations of motion [46]. To assign the final state for each trajectory, the square of the rotational angular momentum $|\boldsymbol{N}'|^2 = N'(N'+1)\hbar^2$ was first calculated, and then the values of N' thereby obtained were rounded to the nearest integer. The Gaussian binning procedure (which involves weighting more heavily those trajectories with the 'correct' rotational action) [47, 48] was also applied in order to determine the state-to-state ($N \rightarrow N'$) cross-sections, but the results were

essentially indistinguishable from those obtained using the conventional histogram-binning procedure (*i.e.* rounding to the nearest integer). Trajectories whose final N' state were found to lie between $N \pm 0.5$ were considered elastic.

At a fixed collision energy, the expression for the inelastic cross-section is

$$\sigma_{N\to N'}(E_{\rm coll}) = \pi b_{\rm max}^2 \frac{\mathcal{N}_{N'}}{\mathcal{N}_{\rm tot}}\,, \tag{10}$$

where $\mathcal{N}_{N'}$ is the number of trajectories ending in state N', and $\mathcal{N}_{\rm tot}$ the total number of trajectories (elastic plus inelastic) from the initial state N. The maximum impact parameter leading to inelastic trajectories was determined by monitoring the change in the rotational quantum number, ΔN, with the criterion that no trajectories with $\Delta N > 0.5$ took place for $b > b_{\rm max}$. Eq. (10) implies that the impact parameter for the i-th trajectory is sampled according to $b^{(i)} = \xi^{1/2} b_{\rm max}$, where ξ is a random number in the $(0, 1)$ interval.

The QCT calculation of the $a^{(k)}(N, N')$ polarization parameters consists simply of determining for each trajectory the asymptotic angle between the initial $\boldsymbol{N}$ and final $\boldsymbol{N'}$ angular momentum vectors [15]:

$$\cos\theta_{NN'} = \frac{\boldsymbol{N}\cdot\boldsymbol{N'}}{|\boldsymbol{N}||\boldsymbol{N'}|}\,. \tag{11}$$

The (de)polarization moments $a^{(k)}(N, N')$ are then calculated as the ensemble average of the corresponding Legendre moments

$$a^{(k)}(N, N') = \langle P_k(\cos\theta_{NN'})\rangle = \frac{1}{\mathcal{N}_{N'}}\sum_{i=1}^{\mathcal{N}_{N'}} P_k(\cos\theta_{NN'}^{(i)})\,, \tag{12}$$

where the sum runs over the ensemble of trajectories ending in a given N' rotational state.

Note that the above treatment is appropriate for QCT calculations in which NO(A) is treated as a closed shell molecule. QCT estimates of the 'open shell' spin-rotation and hyperfine level changing cross-sections, and the associated polarization parameters, were obtained using the tensor opacity formalism described in detail previously [15].

Calculations were also carried out for some sample initial states in which the collision energy was varied in a single batch of trajectories. The method to determine $\sigma_{N\to N'}(E_{\rm coll})$ has been described in refs. [49, 50], and with specific application to the present problem in ref. [12]. The collision energy dependence of the depolarization parameters $a^{(k)}(N, N'; E_{\rm coll})$ can also be evaluated [14]. This allows determination of the thermally averaged depolarization cross-sections $\langle\sigma_{N\to N'}^{(k)}\rangle$ by convoluting the energy dependent collision cross-section

and depolarization parameters with the Maxwell-Boltzmann distribution. These thermally averaged depolarization cross-sections can be compared directly with the experimentally determined values (see Section III).

B. Experimental

The experimental procedures have been described previously [13, 16] and only a brief summary will be given here. Although this is first time that Zeeman quantum beat spectroscopy has been used to study collisional depolarization, experimental details concerning the measurement of orientation using Zeeman quantum beat spectroscopy have been described in a recent publication [16]. The experiments on the depolarization of NO(A) were conducted at 300 K in a slow flow of NO(X) held at a pressure of $\lesssim 1$ mTorr. NO(A) was produced by pulsed Nd:YAG pumped dye laser excitation on the 0-0 band of the NO $A^2\Sigma^+ \leftarrow X^2\Pi$ transition at wavelengths around 226 nm. Spin-rotation levels with $J' = N' - 1/2$, labelled f_2, were excited, with $N' = 2$, 5, 7, 9 and 14 using the $R_{22}\uparrow$ and $S_{21}\uparrow$ transitions. The fluorescence decay traces were recorded on a digital oscilloscope and transferred to a PC for subsequent data acquisition and analysis. The response time of the system was determined to be $\lesssim$20 ns. A Rochon polarizer was used to improve the polarization of the frequency doubled dye laser radiation immediately prior to entering the reaction chamber, and the purity of the polarization was determined to be better than 95% on exiting the chamber.

When conducting alignment experiments, the probe laser radiation was polarized such that its electric vector was aligned 90° to the fluorescence detection direction. The Glan Taylor polarizer used in front of the photomultiplier was aligned parallel to the probe laser propagation axis. In the case of orientation experiments, a photoelastic modulator was employed to convert the linearly polarized laser light to left/right circularly polarized laser light. The (circularly polarized) fluorescence from the excited state NO(A) molecules was then observed through a quarter wave-plate (to convert the circularly polarized light back to linearly polarized light) followed by a Glan Taylor polarizer. The quarter wave-plate is oriented at 45° to the linear polarizer, thereby maximizing the orientation signal, and minimizing the alignment signal, which is also present in the experimental geometry employed. Note that the difference between fluorescence signals obtained with left and right circularly

polarized probe light is only sensitive to angular omentum orientation, whilst the summed signals are only sensitive to population and alignment terms. As shown in the following subsection, the latter has twice the beat frequency (and about one tenth the beat amplitude) that of the orientation signals.

The collider gases, He and Ar, were flowed into the chamber through a separate inlet valve to allow experiments to be performed over a range of partial pressures. The Zeeman quantum beat experiments were performed in a uniform magnetic field of between 0 and 70 Gauss. The field was produced using a pair of matched Helmholtz coils, which were placed inside the reaction chamber, about 2.5 cm away from the interaction region. The centre of the reaction chamber was screened from external magnetic fields by μ-metal shielding. The field was checked using a Hall probe, but could also be determined from the Zeeman beat frequency, since the g_F values for NO(A) are known quite precisely [51]. In the alignment experiments, the axis of the magnetic field was aligned parallel with the fluorescence detection direction [13], while in the orientation experiments the field axis was directed perpendicular to the detection axis, and to the pump laser propagation direction [16]. The quarter wave plate

C. Data analysis

1. *Zeeman quantum beats*

The non-zero nuclear magnetic moments of the nitrogen nucleus ($I = 1$) splits the rotational levels of NO(A) into a number of hyperfine components, characterized by the total angular momentum $\boldsymbol{F} = \boldsymbol{I} + \boldsymbol{j}$. The applied magnetic field lifts the degeneracy of each of these hyperfine sublevels (Zeeman splitting) resulting in $2F + 1$ components characterized by the quantum number M_F (the projection quantum number along the magnetic field direction). The dye laser employed in the present work has a pulse duration $\sim$5 ns, and hence quantum beats between levels split by more than $\sim$30 MHz will be unobservable (see further below). The hyperfine level splittings for NO(A) are of the order of tens of megahertz, so both hyperfine and Zeeman quantum beats could be observed. However, for the levels where it was chosen to observe Zeeman beats ($N' \geqslant 5$), the hyperfine beats were of negligible intensity compared to the Zeeman and inter-manifold beats, and the hyperfine and Zeeman beat data could be analyzed independently.

The fluorescence decays in the Zeeman beat experiments were fit using the following expression [52–55]:

$$I = A\,\mathrm{e}^{-k_\mathrm{p}t} \times \left[1 + \mathrm{e}^{-k_\mathrm{d}t} \sum_F C_F\, \cos\left(2\pi\alpha_F H t + \phi\right)\right] . \tag{13}$$

In this equation, H is the magnetic field strength, ϕ is the phase of the beat signal, defined by the probe laser and detector polarization geometries, and A and C_F are constants defining the total intensity and the relative beat amplitudes, respectively. In the analysis of Zeeman beats, the latter vary only slightly with F for the levels probed in the present work. For NO(A), the three beat frequencies become quite similar for the higher N' levels studies, and in practice the Zeeman quantum beats could then be equally well fit using a single beat frequency. In the Hund's case (b) limit, appropriate to NO(A), the parameter α_F, which defines the beat frequency per unit applied field, can be written to a good approximation [52–55]

$$\alpha_F \simeq 2\,\frac{\mu_0}{h}\,g_F\,, \tag{14}$$

with

$$g_F = g_j \frac{F(F+1) + j(j+1) - I(I+1)}{2F(F+1)}\,, \tag{15}$$

and

$$g_j = g_\mathrm{e} \frac{j(j+1) + S(S+1) - N(N+1)}{2j(j+1)}\,. \tag{16}$$

g_e is the Landé g value for the electron. Note that the quantum numbers are those for NO(A) in its excited electronic states, *i.e.* we have dropped the primes on the quantum numbers in this section.

In a magnetic field an aligned distribution repeats itself twice during a full rotation, while an oriented distribution repeats itself only once. This is manifested in a reduction of the beat frequency α_F by a factor of two in the case of the orientation experiments. Furthermore, it is in fact the difference between the signals obtained using left and right circularly polarized light (I_L and I_R, respectively) that is fit with the expression

$$\mathcal{C} = \frac{I_L - I_R}{I_L + I_R} = \mathrm{e}^{-k_\mathrm{d}t} \sum_F\; C'_F \cos(2\pi\alpha'_F H t + \phi)\,, \tag{17}$$

with $\alpha'_F = \alpha_F/2$, to obtain the disorientation rate constants.

Two phenomenological first order rate constants, k_p and k_d, have been introduced to allow for the decay of population and angular momentum polarization, respectively [56, 57].

The rate constants are dependent on the concentration of the collider, and can both be expressed as sums of rate constants describing collision-free and collisional-induced decay processes

$$\begin{aligned} k_{\mathrm{p}} &= k_0 + k_1\,[\mathrm{M}] \\ k_{\mathrm{d}} &= k_2 + k_3\,[\mathrm{M}]\ . \end{aligned} \tag{18}$$

Note that the population decay, characterized by k_{p}, is associated with processes that remove NO(A), such as fluorescence (k_0) or electronic quenching (k_1), and not with processes such as rotational energy transfer that occur *within* the NO(A) electronic state (see Section III C 3). k_2 is associated with depolarization in the absence of a collider gas, M, which could arise, for example, from field inhomogeneities. Of particular interest to the current work are the rate constants k_3, which account for the collisional depolarization of NO(A). Note that in the following we distinguish between the measured collisional disorientation and 'disalignment' cross-sections using the notation $\sigma_3^{(1)}$ and $\sigma_3^{(2)}$, respectively. Each of these rate constants is discussed in more detail in Section III.

A typical NO(A) alignment Zeeman quantum beat signal, obtained with no added quencher gas present, is shown in Fig. 1. The Zeeman beat amplitude is determined by the alignment of $\boldsymbol{j}$, $A_0^{(2)}$ ($\equiv 2r_0^{(2)}$ of ref. [15]), generated upon absorption of plane polarized light [2, 58], together with the intensity of the fluorescence emitted from the excited state in the particular polarization geometry employed [2, 58, 59]. In the alignment experiments, the fluorescence was observed through a Glan Taylor polarizer without resolving the emission, and the averaging over P↓, Q↓ and R↓ transitions leads to a significant reduction in the strength of the beat signal. With no added collider gas, the beat amplitude can be calculated from the linestrength theory for (1+1) LIF [13, 59]. Because in the Zeeman beat experiments, for the rotational levels chosen, intermanifold beats could not be observed, the linestrength factors have been corrected for hyperfine depolarization [59]. In the case of alignment measurements, after averaging over the hyperfine levels, we obtain a value of $C = 0.05$ (see Eq. 13) for the total relative beat amplitude of the transition shown in Fig. 1, which can be seen to agree quantitatively with the experimental results.

For the orientation experiments, the out-of-phase beats observed from the P↓ and R↓ emission branches nearly cancel, so that almost no beat is present in the unresolved emission. A monochromator has been used to resolve the emission from a single rotational branch to

observe the beat arising from precession of the oriented distribution. A 2400 lines/mm grating was employed with a path length of 30 cm, giving a maximum resolving power of 1.1 Å. The orientation fluorescence decays were recorded using a resolution of 2 Å (for $N = 2$) to 3.4 Å (for $N = 14$) such that fluorescence from a single emission branch only was observed. The resolution employed was chosen to include emission from all accessible rotational levels within the branch while excluding the emission from the neighboring branches. It is also possible to record alignment fluorescence decays using the same resolution of the emission from a single branch. This greatly increases the beat amplitude (as the beats from the different branches no longer cancel), and increases the signal to noise ratio of the quantum beat. We have verified that fits to the alignment data acquired with or without resolution of the emission branch return the same depolarization rate constants. One unavoidable side effect of the partial resolution of the emission is that rotational levels that fluoresce at the edge of the resolved region contribute less than those that fluoresce in the center. However, this is expected to have little effect on the extracted depolarization rates, because the extent of rotational energy transfer within the timescale of the fluorescence decay is relatively small. This is verified by similarity of the alignment rate constants determined with and without emission branch resolution.

For each rovibronic transition, a series of between 6 and 8 fluorescence decay curves obtained as a function of collider concentration were fitted globally, using the signal amplitudes, A, the relative beat amplitudes, C_F, the magnetic field H, the phase ϕ, and the four rate coefficients as adjustable parameters (see Section III B). Errors were estimated using a Monte Carlo error routine described elsewhere [60].

2. Hyperfine quantum beats

As noted above, for NO(A) the hyperfine splitting is sufficiently small for hyperfine levels of a given j to be excited coherently. The alignment induced by photon absorption then oscillates in time between $\boldsymbol{j}$ and $\boldsymbol{I}$ due to coupling with the nuclear spin. The time dependence of the polarization of both $\boldsymbol{j}$ and $\boldsymbol{I}$ have been discussed recently by Rakitzis and coworkers [61], and in the former case is

$$A_0^{(2)}(j,t) = G^{(2)}(j,t)\, A_0^{(2)}(j,t=0)\,, \tag{19}$$

where

$$G^{(k)}(j,t) = \sum_{F,F'} \frac{(2F+1)(2F'+1)}{(2I+1)} \left\{ \begin{array}{ccc} F' & F & k \\ j & j & I \end{array} \right\}^2 \cos\left[(E_F - E_{F'})t/\hbar\right], \tag{20}$$

where E_F represents the hyperfine energy levels of NO(A). An example of the hyperfine quantum beat obtained without quencher gas present, and in the absence of an applied magnetic field, is shown in Fig. 2.

The time dependent LIF signals were fitted to an expression similar to that given in Eq. (13)

$$I = A\,\mathrm{e}^{-k_\mathrm{p}t} \times \left[1 + \mathrm{e}^{-k_\mathrm{d}t} \sum_F C''_F \cos\left(2\pi\omega_F t + \phi\right)\right], \tag{21}$$

where ω_F are the hyperfine splitting frequencies of NO(A). The latter were treated as adjustable parameters in the fits to the data, as were the beat amplitudes C''_F. As with the Zeeman beat data, the factor of two is necessary to account for the different repetition rate on rotation of an aligned distribution versus an oriented distribution. The hyperfine beat frequencies obtained in the present work for the f_2 levels of NO(A, $v' = 0$) are given in Table I, where they are compared with recent data from McCormack and Sarajlic for the f_1 levels [62]. The beat amplitudes could also be calculated from a knowledge of the time-dependent alignment and the LIF linestrengths discussed above [59]. Hyperfine depolarization corrections were not applied in the case when the hyperfine beat signal was resolved [59]. The comparison between the experimental and calculated beat signal is shown in Fig. 2, and demonstrates that, as with the Zeeman quantum beats, and in the absence of significant collisional depopulation or depolarization, the beat intensities are well reproduced by the calculations.

III. RESULTS

A. Calculation results

In the following section the experimental depolarization cross-sections will be compared with those obtained in the fixed energy 'open shell' QCT calculations. To verify that these are a reliable approximation to the true QM thermally averaged cross-sections, the fixed energy QCT results are compared with both fixed energy c–s QM results, and thermally averaged QCT results.

The left panels of Fig. 3 show the state-to-state integral (top), disorientation (middle), and disalignment (bottom) cross-sections obtained from fixed energy QCT, thermally averaged QCT, and fixed energy c–s QM calculations for NO(A) + Ar from initial state $N = 2$. All the calculations in this figure treat NO(A) as a closed shell molecule. The panels on the right display the thermal and fixed energy QCT, and fixed energy c–s QM total depolarization cross-sections summed over all final states. Besides the expected alternation in the magnitude of the c–s QM state-to-state depolarization cross-sections with N' shown in the upper panels, which arises due to the near homonuclear character of the NO molecule, there is very little difference between the various sets of results. In particular, the depolarization cross-sections are very well reproduced by the fixed energy QCT data. This indicates not only that the QCT values are a good approximation to the c–s QM data, but also that the dynamics are similar over the range of collision energies sampled at room temperature. As a consequence, in the remainder of the paper it is reasonable to compare the thermally averaged experimental data directly with their fixed energy QCT counterparts.

In the limit at which the electron spin and nuclear spin can be treated as spectators during the course of the collision, it is possible to determine 'open shell' cross-sections and depolarization moments from the (intrinsically closed shell) QCT calculations [12, 15]. Fig. 4 illustrates the efficacy of this strategy, but now comparing the open shell cross-sections for electron spin conserving and changing collisions for $N = 2$ obtained in the o–s QM calculations with those derived using the 'open shell' QCT tensor opacity formalism described previously [15]. The figure includes both rotational energy transfer (top panels) and collisional depolarization cross-sections. Apart from the oscillatory nature of the o–s QM cross-sections with N', the agreement between the exact o–s QM and the 'open shell' QCT calculations is very good, particularly so for the depolarization cross-sections. For this reason, in the following we will compare the experimentally determined depolarization cross-sections for NO(A) + Ar and NO(A) + He with those obtained from the fixed energy 'open shell' QCT calculations. Note that once the o–s QM data are summed over final and average over initial spin-rotation changing state they yield almost identical results to the c–s QM calculations.

B. Fluorescence decays and quantum beats

Experimental fluorescence decays obtained at a series of He quencher gas pressures are shown in Fig. 5 for the case of hyperfine beats. Also shown are the time-dependent beat amplitudes, which emphasize the decay of the beat intensity, both with time and with bath gas pressure. Fig. 6 displays a series of time dependent experimental (orientation) Zeeman quantum beat amplitudes at a series of Ar quencher gas pressures, as well as the fits to these data.

Apart from the depolarization cross-sections of interest, the fits to the data yield a number of other rate coefficients, characterizing various population and polarization loss processes. The experimentally determined values of the fluorescence lifetimes for NO(A) were found to lie within a few percent of the values given by the program LIFBASE [63] and by other recent measurements by Settersten *et al.* [64]. A lifetime of 210 ± 2 ns was obtained for the f_2 levels in the range $N' = 2 - 14$, which agrees favourably with the radiative lifetime of 205 ± 7 ns recommended by Luque and Crosley [65] obtained from similar types of measurements. Unlike our previous work on the depolarization of OH(A) by water [13], electronic quenching rate constants for NO(A) with Ar and He were too slow to be measured over the timescales and pressure ranges used to study depolarization. The cross-section for electronic quenching of NO(A) with He and Ar are $0.02\,\text{Å}^2$ and $0.01\,\text{Å}^2$ [66], respectively. Thus, with maximum pressures of $\sim$800 mTorr, electronic quenching in these experiments can be safely neglected.

Some depolarization is observed to take place even in the absence of any collisions. As in our previous work [13], the rate constant k_2 that accounts for any such depolarization was found to scale linearly with the Larmor frequency. This could arise for a number of reasons, but most likely reflects modest field inhomogeneities that are present even with the use of μ-metal shielding. The k_2 values at the fields employed were typically smaller than half the loss rate due to fluorescence, and thus can be regarded as a relatively minor decay channel, and in some cases k_2 could be safely neglected altogether. In the case of the hyperfine quantum beat data for NO(A), k_2 values were typically $k_2 \lesssim 1.5 \times 10^6\,\text{s}^{-1}$, which compares with a fluorescence decay rate of $4.9 \times 10^6\,\text{s}^{-1}$.

C. Depolarization cross-sections

1. *Raw data*

The depolarization cross-sections obtained from simultaneous fits to the decay curves obtained as a function of pressure are presented graphically in Fig. 7, where error bars refer to 95% confidence limits. Notice that there is reasonable agreement between the measurements involving hyperfine and Zeeman quantum beats. The experimental cross-sections are also given in Tables II to V along with the QCT 'open shell' calculated depolarization cross-sections, resolved into their contributions from elastic and inelastic collisions. Note that the QCT data presented in these tables is in excellent agreement with the o-s QM data (as illustrated already in Fig. 4). The row labeled 'Elastic' refers to the calculated depolarization cross-sections arising from collisions which change the direction of $\boldsymbol{j}$, but not its magnitude. These collisions are those for which $\Delta N = \Delta j = 0$. The QCT inelastic depolarization cross-sections are given by the sum over all other final spin-rotation states, N', j', and thus include all processes in which the rotational level changes, *i.e.* $N' \neq N$ and $j' \neq j$.

Figs. 8 and 9 compare these total 'open shell' QCT calculated integral (top panel), orientation (middle panel), and alignment (bottom panel) depolarization cross-sections with the experimental values for NO(A) + Ar and He, respectively. The total rotational energy transfer cross-sections shown in the top panels of the figures have been taken from the literature [67–69]. The calculated depolarization cross-sections agree qualitatively with the experimental values, although they tend to slightly underestimate them, for reasons discussed further in the following section. The agreement between the experimental and QCT depolarization cross-section results, however, is particularly good in the case of NO(A) with He (Fig. 9). The QCT integral rotational energy transfer cross-sections also agree well with the experimental values available from the literature [68] for NO(A) + He. For NO(A) + Ar (Fig. 8), the experimental rotational energy transfer cross-section previously determined at low N [68] is significantly larger than the QCT calculated result, although the values obtained at higher N [67, 69] are in better agreement with the current theory.

A key result from the present study is that the depolarization cross-sections, both for disorientation and disalignment, are significantly smaller than the total rotational energy transfer cross-sections. This difference is even more pronounced for NO(A) with He than

for NO(A) with Ar. We return to this point in Section IV, once we have considered in detail the dephasing effects of rotational energy transfer collisions.

2. Quantum beat dephasing

Depolarization of the observed fluorescence signal may take place *via* both elastic and inelastic collisions within the $v = 0$ level of NO(A) (see Section III B). The RET collisions populate states of NO(A) with different j, N, S and F quantum numbers, which have different g_F-values and hence precession rates in a magnetic field [13, 14]. Thus even in the absence of depolarization, dephasing of the beat signal will occur due to the overlap of several oscillatory signals with different beat frequencies, arising from the collisional population of several different NO(A) rotational states. Here we use the term dephasing to denote this unwanted contribution to the loss of beat signal, to distinguish it from the elastic and inelastic collisional depolarization effects of interest.

An important factor in the dephasing mechanism is the degree to which RET collisions populate different spin-rotation states to that initially excited on the timescale of the experiment. As illustrated in the Fig. 10, for NO(A) the f_1 and f_2 spin-rotation states have g_F values and hyperfine couplings of different signs, leading to a change in the energy level ordering of the Zeeman and hyperfine levels. When a spin-rotation changing collision occurs, it leads to a change in the direction of precession in the magnetic field, thus potentially resulting in signal dephasing. Neighbouring rotational states within the same spin-rotation manifold have quite similar g_F values and hyperfine splittings, and, therefore, RET collisions that do not lead to a change in spin-rotation level will have a more modest dephasing effect. In passing, it is worth mentioning that spin-rotation state and hyperfine level changing collisions have a similar dephasing effect on the depolarization signal when the latter are monitored by observing the decay of hyperfine quantum beats, in the *absence* of a magnetic field. In this case population of different spin-rotation levels to those initially excited would cause a change in the direction of 'flow' of alignment between $\boldsymbol{j}$ and $\boldsymbol{I}$ [61].

In order to quantify the extent to which dephasing by inelastic processes, including spin-rotation and hyperfine changing collisions, influences the depolarization cross-sections reported in Table I, we have performed a series of detailed simulations of the NO(A) + Ar Zeeman quantum beat experiments using a Monte Carlo procedure to integrate the kinetic

equations, the details of which are discussed in ref. [14]. Matrices of the rate constants and depolarization moments were calculated up to $N = 15$, which was found to be sufficient to describe the rotational energy transfer processes for initially populated states up to $N = 14$. In the present work, we use the results of the 'open shell' QCT calculations obtained at a fixed collision energy of 39 meV, which as we have seen provide a very good approximation to the exact quantum mechanical scattering calculations of the thermal rate coefficients [12, 15]. Because the effects of electron spin can be treated accurately within an energy sudden approximation over a wide range of energies, there are similar levels of agreement between the QM and QCT calculations, irrespective of whether NO(A) is treated as an open shell or closed shell species.

The simulations generate output decay curves as a function of quencher gas pressure similar to the data obtained experimentally. The simulated decays were then fit using the same programs employed to analyze the experimental data. Thus, for a given input energy transfer and depolarization rate constant matrix, the fits to the simulated decay curves returned values of the depolarization rate constant k_3, with the differences between the input ($k_N^{(2)}$) and output (k_3) depolarization rate constants reflecting the importance of dephasing effects induced by state-changing collisions.

3. Simulation results and comparison with experiment

The experimental, calculated, and simulated depolarization cross-sections for NO(A) + Ar are compared in Tables II and IV. As noted above, the tables also give the input total depolarization cross-sections used in the simulations (*i.e.* the depolarization cross-sections, $\sigma_N^{(k)}$, calculated by the 'open shell' QCT methods at a fixed collision energy of 39 meV). Hyperfine and spin-rotation level changing collisions have the smallest (most negative) depolarization parameters, $\langle a^{(k)}(j)\rangle$, leading to larger depolarization rate constants [14, 15], and also cause the maximum dephasing effect, due to the change in sign in g_F for different spin-rotation levels. However, the probability of undergoing a hyperfine/spin-rotation changing collision is dependent on the probability of a large change in the direction of $\boldsymbol{N}$ during the course of the collision, and so their role is less important when the direction of $\boldsymbol{N}$ tends to be conserved. Conversely, collisions in which the hyperfine/spin-rotation level does not change (although N may still change) are less depolarizing, but the cross-sections for

these processes tend to be larger, because they do not require the direction of $\boldsymbol{N}$ to change so dramatically. The interplay between these two factors determines whether depolarization occurs predominantly from hyperfine/spin-rotation changing or hyperfine/spin-rotation conserving collisions.

In Fig. 11 we compare experimental depolarization cross-sections, $\sigma_3^{(k)}$, for NO(A) + Ar with the total depolarization cross-sections derived from the fits to the simulations using the 'open shell' QCT data. The agreement between the two sets of results is noticeably better than in Fig. 8, where the dephasing has been neglected, particularly for the NO(A) + Ar data. However, the additional effect of this dephasing due to the population of final states with different g_F values is small compared to the loss of beat amplitude caused by collisional depolarization. This can be attributed to the relatively small cross-sections for spin-rotation and hyperfine changing collisions for NO(A) + Ar. Recall that for such collisions the signs of the g_F values are reversed. In the absence of significant spin-rotation or hyperfine changing collisions, the g_F values change very little and so dephasing is slow on the timescale of the fluorescence decay. Although we have not performed a detailed simulation for NO(A) + He, the cross-section data shown in Fig. 9 provides strong support for the view that dephasing effects in that system will also be very small.

IV. DISCUSSION

A. Disorientation versus disalignment

As can be seen from Fig. 8 and Fig. 9, the disorientation cross-sections for both NO(A) + Ar and NO(A) + He tend to be a little smaller than the disalignment cross-sections. This behaviour is expected for impulsive type collisions since it is much harder to change the sense of rotation than it is the axis of rotation. Similar behaviour has recently been observed by Costen and McKendrick and coworkers in the elastic depolarization of OH(X) by Ar and He [70]. Classically, such behaviour is expected for impulsive collisions since $P(\theta_{jj'})$ is then likely to peak at angles $\theta_{jj'} \sim 0$, and be a monotonically decreasing function as $\theta_{jj'}$ increases. Large changes in $\theta_{jj'}$ would therefore be disfavoured. If the collisions were not impulsive, as might be the case for a potential energy surface with a deep well, $\theta_{jj'}$ would range more uniformly between 0 and π, and $a^{(1)}(j)$ and $a^{(2)}(j)$ would both take values closer to zero.

Under these conditions, the depolarization cross-sections would have magnitudes similar to the collision cross-sections, since each collision would randomize the direction of $\boldsymbol{j}$. This is reminiscent of the strong depolarization observed in collisions of OH(A) with Ar [14, 15], where the well-depth in the potential energy surface is around $1600\,\mathrm{cm}^{-1}$ [12].

B. Comparisons with RET cross-sections

On comparison of the RET and depolarization cross-sections presented in Figs. 8 and 9, it can be seen that depolarization of an aligned or oriented distribution of angular momenta is a less efficient process than rotational energy transfer by collision. This corresponds to a tendency to conserve the direction of $\boldsymbol{j}$ to some degree during the collision. This would be expected to be the case in a 'hard-shell', impulsive collision model, and so the fact that we observe this behavior experimentally and theoretically is a reflection of the relatively unattractive nature of the PESs involved [41]. This behaviour should be contrasted with that for OH(A) + Ar, where the depolarization cross-sections (and associated rate constants) are roughly equal to the corresponding RET cross-sections [12, 14, 15]. As noted above, this corresponds to the total randomization of the direction of $\boldsymbol{j}$ after a single collision. This is associated with a strongly attractive PES in which the diatom is pulled into an energetically favorable configuration with the collision partner no matter what the initial direction of $\boldsymbol{j}$.

As noted in Section I, in the limit in which the electron spin, $\boldsymbol{S}$, can be treated as a spectator during the collision, the ratio of the spin-orbit changing to spin-orbit conserving RET cross-sections is also determined by the distribution of $\theta_{jj'}$ [15]. The expression for the cross-sections can be split into a closed-shell *dynamical* part and an open-shell *geometric* (angular momentum recoupling) part [15, 27–30], and the open-shell RET cross-sections $\sigma_{j\rightarrow j'}$ and accompanying depolarization moments $a^{(k)}(j,j')$ are determined by the extent to which $\boldsymbol{N}$ is reoriented on collision. There emerges a direct correlation between the importance of spin-orbit changing collisions and the magnitude of the depolarization cross-sections relative to the collision cross-section. That the spin-orbit changing cross-sections for OH(A) with Ar are significantly larger than those for NO(A) with Ar and He reflects further the fact that the former collisions tend to change the direction of $\boldsymbol{N}$ much more dramatically.

C. Comparison of depolarization data with previous work

The depolarization cross-sections obtained in this work for NO(A) with He and Ar can be compared with the elastic (alignment) depolarization cross-sections measured by McKendrick and Costen and coworkers [17, 70–75] for OH(X) with Ar and He. The PES's for NO(A) and OH(X) with either collision partner have similar degrees of attractive and repulsive character, and so one might expect their depolarization cross-sections to be comparable. One major difference between OH(X) and NO(A) is that the spacing between the rotational energy levels is much greater in OH(X) than in NO(A). As a consequence, elastic scattering in OH(X) + Rg collisions plays a much more important role relative to inelastic scattering than it does for NO(A) + Rg. These differences appear also to be manifested in the relative magnitudes of the depolarization cross-sections.

In the case of OH(X) + Ar, the experiments of McKendrick and Costen and coworkers [70], together with the recent QM calculations of Dagdigian and Alexander [34–36], suggest elastic (alignment) depolarization cross-sections for $N = 2, j = 2.5$ of around $20\,\text{Å}^2$. For NO(A) + Ar, the 'open shell' QCT calculated elastic (alignment) depolarization cross-section determined here is only around $8.0\,\text{Å}^2$ for the initial state $N = 2, j = 1.5$ (it is $8.5\,\text{Å}^2$ for the other spin-rotation state $N = 2, j = 2.5$). Note, however, that this value neglects the contribution from pure spin-rotation changing collisions. The closed shell QM calculations yield a value of $18\,\text{Å}^2$ for the elastic depolarization cross-section. The larger value for OH(X) relative to NO(A) reflects in part the greater propensity for elastic scattering relative to inelastic scattering rather than simply an enhanced propensity to change the direction of $\boldsymbol{j}$ in the case of OH(X) + Ar. These values for the *elastic* depolarization cross-sections can be contrasted with the present experimentally measured *total* depolarization cross-sections of $127\,\text{Å}^2$ for NO(A) + Ar and $41\,\text{Å}^2$ for NO(A) + He (again for initial state $N = 2$). Elastic depolarization in NO(A) with Ar and He is less significant relative to OH(X) (or indeed OH(A)) with Ar and He due to the aforementioned differences in rotation energy level spacings.

In a very recent paper Dagdigian and Alexander [36] have compared the elastic depolarization and RET cross-sections of OH(X) and NO(X) with Ar. They observed that the difference potential, V_{diff}, plays a significant role in the elastic depolarization of OH(X) by Ar, and that treating the $^2\Pi$ radicals as closed-shell molecules can lead to a significant dif-

ference in the predicted elastic depolarization cross-sections. The added complexity arising from the electronic structure of OH(X) and NO(X), compared with OH(A) and NO(A), is therefore an additional factor that needs to be considered when comparing the depolarization cross-sections for the ground and excited state molecules. The closed shell elastic depolarization cross-section presented in Fig. 3 for NO(A)+Ar for $N = 2$ is about a factor of two larger than the closed shell elastic depolarization cross-sections present by Dagdigian and Alexander for NO(X, $N = 2$) + Ar (see Fig. 4 of Ref. [36]), presumably reflecting differences in PESs employed for the electronic ground and excited state systems.

D. Kinematics versus dynamics

The depolarization cross-sections for NO(A) with Ar are invariably larger than those for NO(A) with He. This difference would perhaps be expected to arise from the increased momentum of the Ar atom relative to the He atom at a given collision energy. However, differences in the PES's for the two systems might also play a role in determining their differing depolarization cross-sections. In particular, the fact that the interaction between NO(A) and He is almost purely repulsive [41, 76, 77] might account partly for the very low depolarization cross-sections observed for this system. QCT calculations were used to quantify the relative importance of the mass of the collision partner and the PES in determining the observed depolarization cross-sections. Trajectories were first run for initial state $N = 7$ for NO(A) + ^{40}Ar and NO(A) + ^{4}He to determine the depolarization cross-sections shown in Figs. 8 and 9. Further trajectories were then run for $N = 7$ using the same PES's, but swapping the mass of the collision partners - the resulting systems shall be denoted NO(A) + ^{4}Ar and NO(A) + ^{40}He.

Fig. 12 shows the RET cross-sections and the (alignment) depolarization moments and cross-sections for the four PES/collision partner mass combinations. As can be seen, changing the mass of the collision partner has only a small effect on the RET cross-sections compared to changing the PES. The depolarization moments are roughly equally sensitive to the mass of the collision partner and the PES used (for example, the change on going from NO(A) + ^{40}Ar to NO(A) + ^{4}Ar is similar to that on going from NO(A) + ^{40}Ar to NO(A) + ^{40}He). These factors combine to give the observed behavior of the depolarization cross-sections. As expected intuitively, the heavier collision partners have larger depolarization

cross-sections than the lighter ones, but this effect does not reverse the ordering imposed by the PES (indeed for the NO(A) + He PES, the total depolarization cross-sections for NO(A) with ^{4}He or ^{40}He are quite similar). It seems likely that that the relative importance of kinematic factors and the PES will vary somewhat with initial N, with the attractive part of the potential playing a particularly important role for low ΔN collisions at low initial N. It is also worth mentioning that since the depolarization cross-sections are given by $\sigma^{(k)} = \sigma \times \left[1 - a^{(k)}\right]$ (cf. Eq. (5)), any variation in the depolarization moments $a^{(k)}$ will have the largest impact on the cross-sections when $a^{(k)}$ is close to its limiting value of +1, as is the case for high initial N in collisions of NO(A) with He. As the depolarization moments get closer to zero (as would be the case in a highly depolarizing system such as OH(A)+Ar), any change in their value has a less pronounced effect on the depolarization cross-sections, and this will reduce the importance of kinematic effects in determining the depolarization cross-sections.

V. CONCLUSIONS

In the present paper we show how Zeeman and hyperfine quantum beat spectroscopy can be used to measure the collisional angular momentum depolarization rates of electronically excited molecules. In both cases the beat amplitude at short times, in the absence of collisions, is well-described by existing linestrength theory for (1+1) LIF. We show how the application of a weak magnetic field makes the LIF signal sensitive to both angular momentum alignment and orientation. The subsequent pressure dependent decay of the beat amplitude is used to extract depolarization rate constants and estimates of cross-sections for both orientation and alignment. In particular, depolarization rate constants and velocity averaged cross-sections are provided for NO($A^2\Sigma^+$) in the presence of He and Ar. In both systems, the cross-sections for loss of orientation are significantly smaller than those for collisional loss of alignment. The present depolarization experiments are shown to provide a direct and detailed probe of the character of the molecular collisions. A key result of the paper is that for NO(A) with Ar, and particularly with He, collisional depolarization cross-sections are significantly smaller than the cross-sections for rotational energy transfer. Collisions tend to be more impulsive type encounters, that preferentially preserve the direction of the angular momentum $\boldsymbol{j}$. This behavior should be contrasted with OH(A)

depolarization by Ar, which was found previously to proceed with a rate comparable too, or larger than, that for rotational energy transfer, consistent with a significant tilting of $\boldsymbol{j'}$ away from $\boldsymbol{j}$ on collision [14, 15].

Acknowledgments

The support from EPSRC (to M.B. *via* Programme Grant No. EP/G00224X/1) is gratefully acknowledged. FJA acknowledges the financial support by the Spanish Ministry of Education and Science under the grant CTQ2008-02578/BQU. J.K. would like to gratefully acknowledge financial support from the U.S. National Science Foundation under grant CHE-0413743 and of the University Complutense de Madrid/Grupo Santander under the programme of "Movilidad de Investigadores Extranjeros".

---

[1] R. N. Zare, *Angular Momentum, Understanding Spatial Aspects in Chemistry and Physics* (John Wiley and Sons, 1988).

[2] K. Blum, *Density Matrix Theory and Applications* (Plenum Press, New York, 2000).

[3] U. Fano and J. H. Macek, Review of Modern Physics **45**, 553 (1973).

[4] S. K. Kim and D. R. Herschbach, Faraday Discuss. Chem. Soc. **84**, 159 (1987).

[5] M. P. de Miranda and D. C. Clary, J. Chem. Phys. **106**, 4509 (1997).

[6] C. H. Greene and R. N. Zare, Ann. Rev. Phys. Chem. **33**, 119 (1982).

[7] A. J. Orr-Ewing and R. N. Zare, Ann. Rev. of Phys. Chem. **45**, 315 (1994).

[8] R. N. Dixon, J. Chem. Phys. **85**, 1866 (1986).

[9] A. J. Alexander, M. Brouard, K. S. Kalogerakis, and J. P. Simons, Chem. Soc. Rev. **27**, 405 (1998).

[10] M. Brouard, P. O'Keeffe, and C. Vallance, J. Phys. Chem. A **106**, 3629 (2002).

[11] W. K. Roeterdink, K. E. Strecker, C. C. Hayden, M. H. M. Janssen, and D. W. Chandler, J. Chem. Phys. **130**, 13405 (2009).

[12] J. Kłos, M. H. Alexander, M. Brouard, C. J. Eyles, and F. J. Aoiz, J. Chem. Phys. **129**, 054301 (2008).

[13] M. Brouard, A. Bryant, I. Burak, F. Quadrini, I. A. Garcia, and C. Vallance, Mol. Phys. **103**,

1693 (2005).

[14] M. Brouard, A. Bryant, Y.-P. Chang, R. Cireasa, C. J. Eyles, A. M. Green, S. Marinakis, F. J. Aoiz, and J. Kłos, J. Chem. Phys. **130**, 044306 (2009).

[15] F. J. Aoiz, M. Brouard, C. J. Eyles, J. Kłos, and M. P. de Miranda, J. Chem. Phys. **130**, 044305 (2009).

[16] M. Brouard, H. Chadwick, Y.-P. Chang, R. Cireasa, and C. J. Eyles, Physica Scripta **In press** (2009).

[17] M. L. Costen, S. Marinakis, and K. G. McKendrick, Chem. Soc. Rev. **37**, 732 (2008).

[18] E. A. Brinkman and D. R. Crosley, J. Phys. Chem. A **108**, 8084 (2004).

[19] C. F. Gorter, Naturwissenscaften **26**, 140 (1938).

[20] R. J. van Brunt and R. N. Zare, J. Chem. Phys. **48**, 4304 (1968).

[21] L. D. A. Siebbeles, M. Glass-Maujean, O. S. Vasyutinskii, J. A. Beswick, and O. Roncero, J. Chem. Phys. **100**, 3610 (1994).

[22] A. P. Clark, M. Brouard, F. Quadrini, and C. Vallance, Phys. Chem. Chem. Phys. **8**, 5591 (2006).

[23] A. P. Clark, R. Cireasa, M. Brouard, F. Quadrini, and C. Vallance, in *Molecular Reaction and Photodissociation Dynamics in the Gas Phase",* Eds. P. D. Kleiber and K. C. Lin (Research Signpost, India, in press, 2007).

[24] A. G. Suits and O. S. Vasyutinskii, Chem. Rev. **108**, 3706 (2008).

[25] A. Brown, G. G. Balint-Kurti, and O. S. Vasyutinskii, J. Phys. Chem. A **108**, 7790 (2004).

[26] R. T. Carter and J. R. Huber, Chem. Soc. Rev. **29**, 305 (2000).

[27] M. H. Alexander and S. L. Davis, J. Chem. Phys. **78**, 6754 (1983).

[28] G. C. Corey and F. R. McCourt, J. Phys. Chem. **87**, 2723 (1983).

[29] G. C. Corey and A. D. Smith, J. Chem. Phys. **83**, 5663 (1985).

[30] G. C. Corey, M. H. Alexander, and J. Schaefer, J. Chem. Phys. **85**, 2726 (1986).

[31] E. A. Moore and W. G. Richards, Phys. Scr. **3**, 223 (1971).

[32] C. Amiot and J. Verges, Chem. Phys. Lett. **66**, 570 (1979).

[33] B. Follmeg, P. Rosmus, and H.-J. Werner, J. Chem. Phys. **93**, 4687 (1990).

[34] P. Dagdigian and M. H. Alexander, J. Chem. Phys. **130**, 094303 (2009).

[35] P. Dagdigian and M. H. Alexander, J. Chem. Phys. **130**, 164315 (2009).

[36] P. Dagdigian and M. H. Alexander, J. Chem. Phys. **130**, 204304 (2009).

[37] M. P. de Miranda, F. J. Aoiz, L. Bañares, and V. S. Rábanos, J. Chem. Phys. **111**, 5368 (1999).

[38] M. P. de Miranda and F. J. Aoiz, Phys. Rev. Lett. **93**, 083201 (2004).

[39] M. P. de Miranda, F. J. Aoiz, M. Brouard, and V. Sáez-Rábanos, J. Chem. Phys. **121**, 4509 (2004).

[40] J. Aldegunde, F. J. Aoiz, and M. P. de Miranda, Phys. Chem. Chem. Phys. **10**, 1139 (2008).

[41] J. Kłos, M. H. Alexander, R. Hernndez-Lamoneda, and T. G. Wright, J. Chem. Phys. **129**, 244303 (2008).

[42] HIBRIDON is a package of programs for the time-independent quantum treatment of inelastic collisions and photodissociation written by M. H. Alexander, D. Manolopoulos, H.-J. Werner, and B. Follmeg, with contributions by P. F. Vohralik, D. Lemoine, G. Corey, R. Gordon, B. Johnson, T. Orlikowski, A. Berning, A. Degli-Esposti, C. Rist, P. Dagdigian, B. Pouilly, G. van der Sanden, M. Yang, F. de Weerd, S. Gregurick, and J. Klos.

[43] D. E. Manolopoulos, J. Chem. Phys. **85**, 6425 (1986).

[44] M. H. Alexander and D. E. Manolopoulos, J. Chem. Phys. **86**, 2044 (1987).

[45] The MOLSCAT computer code, version 14, by Hutson J. M. and Green S., (Collaborative Computational Project No. 6 of the Science and Engineering Research Council, United Kingdom, 1994).

[46] F. J. Aoiz, J. E. Verdasco, V. J. Herrero, V. S. Rábanos, and M. H. Alexander, J. Chem. Phys. **119**, 5860 (2003).

[47] L. Bonnet and J.-C. Rayez, Chem. Phys. Lett. **397**, 106 (2004).

[48] L. Bañares, F. J. Aoiz, P. Honvault, B. Bussery-Honvault, and J. M. Launay, J. Chem. Phys. **118**, 565 (2003).

[49] F. J. Aoiz, L. Bañares, T. Díez-Rojo, V. J. Herrero, and V. S. Rábanos, J. Phys. Chem. **100**, 4071 (1996).

[50] F. J. Aoiz, L. Bañares, and V. J. Herrero, J. Chem. Soc. Faraday Trans. **94**, 2483 (1998).

[51] K. R. German, R. N. Zare, and D. R. Crosley, J. Chem. Phys. **54**, 4039 (1971).

[52] P. Lebow, F. Raab, and H. Metcalf, Phys. Rev. Lett. **42**, 85 (1979).

[53] F. Raab, T. Bergman, D. Lieberman, and H. Metcalf, Optics Lett. **5**, 427 (1980).

[54] F. Raab, T. Bergman, D. Lieberman, and H. Metcalf, Phys. Rev. A **24**, 3120 (1981).

[55] J. Xin, I. Ionescu, D. Kuel, and S. A. Reid, Chem. Phys. **291**, 61 (2003).

[56] P. J. Brucat and R. N. Zare, J. Chem. Phys. **78**, 100 (1983).

[57] P. J. Brucat and R. N. Zare, J. Chem. Phys. **81**, 2562 (1984).

[58] R. N. Zare, Berichte der Bunsen-Gesellschaft **86**, 422 (1982).

[59] A. C. Kummel, G. O. Sitz, and R. N. Zare, J. Chem. Phys. **88**, 7357 (1988).

[60] M. Brouard, I. Burak, S. D. Gatenby, D. Hart, and D. Minayev, J. Chem. Phys. **111**, 11335 (1999).

[61] L. Rubio-Lago, D. Sofikitis, A. Koubenakis, and T. P. Rakitzis, Phys. Rev. A **74**, 042503 (2006).

[62] E. F. McCormack and E. Sarajlic, Phys. Rev. A **63**, 023406 (2001).

[63] "*LIFBASE: Database and simulation program (v. 1.6).*" J. Luque and D. R. Crosley, SRI International Report MP 99-009, (1999).

[64] T. B. Settersten, B. D. Patterson, and J. A. Gray, J. Chem. Phys. **124**, 234308 (2006).

[65] J. Luque and D. R. Crosley, J. Chem. Phys. **112**, 9411 (2000).

[66] J. B. Nee, C. Y. Juan, J. Y. Hsu, J. C. Yang, and W. J. Chen, Chem. Phys. **300**, 85 (2004).

[67] A. V. Smith and A. W. Johnson, Chem. Phys. Lett. **93**, 608 (1982).

[68] T. Imajo, K. Shibuya, and K. Obi, Chem. Phys. Lett. **137**, 139 (1987).

[69] T. Ebata, Y. Anezaki, M. Fujii, N. Mikami, and M. Ito, Chem. Phys. **84**, 151 (1984).

[70] G. Paterson, S. Marinakis, M. L. Costen, K. G. McKendrick, and J. Kłos, J. Chem. Phys. **129**, 074304 (2008).

[71] M. L. Costen and K. G. McKendrick, J. Chem. Phys. **122**, 164309 (2005).

[72] H. J. Crichton, M. L. Costen, and K. G. McKendrick, J. Chem. Phys. **119**, 9461 (2003).

[73] M. L. Costen, H. J. Crichton, and K. G. McKendrick, J. Chem. Phys. **120**, 7910 (2004).

[74] S. Marinakis, G. Paterson, J. Kłos, M. L. Costen, and K. G. McKendrick, Phys. Chem. Chem. Phys. **9**, 4414 (2007).

[75] S. Marinakis, G. Paterson, G. Richmond, M. Rockingham, M. L. Costen, and K. G. McKendrick, J. Chem. Phys. **128**, 021101 (2008).

[76] J. Loreille, S. D. Gamblin, S. E. Daire, T. G. Wright, and D. M. Smith, J. Chem. Phys. **113**, 7224 (2000).

[77] S. D. Gamblin, S. E. Daire, J. Lozeille, and T. G. Wright, Chem. Phys. Lett. **325**, 232 (2000).

[78] T. Bergeman and R. N. Zare, J. Chem. Phys. **61**, 4500 (1974).

N'	ν_1	ν_2	Ref. [62]
2	12.3(4)	16.3(3)	16.1(6) 35(1)
3	16.0(3)	18.0(3)	16.9(6) 33(1)
4	17.3(3)	-	17.8(6) 33(1)
5	17.5(4)	-	
6	19.3(4)	-	

TABLE I: Hyperfine beat frequencies (in MHz) for the f_2 ($J = N-1/2$) levels of NO($A^2\Sigma^+, v' = 0$). The numbers in brackets are the 1σ errors, and refer to the least significant figure. For $N' \geq 4$ it was difficult to resolve more than one beat frequency, and only one is reported for these levels. The final column compares the present frequencies with the beat frequencies reported for the f_1 ($J = N + 1/2$) levels of NO(A) by McCormack and Sarajlic [62].

N'	2	5	7	9	14
Hyperfine	127 ± 39	65 ± 20			
Zeeman		52 ± 18	43 ± 13	36 ± 9	11 ± 2
Simulation	105	59			21
QCT total	84.0	52.6	38.8	27.6	13.4
QCT elastic	8.0	5.8	5.9	5.4	4.9
QCT inelastic	76.0	46.8	32.9	22.2	8.5

TABLE II: Experimental thermal (300 K) depolarization cross-sections for 'disalignment', $\sigma_3^{(2)}/\text{Å}^2$, of NO(A) by Ar. The experimental data were obtained using (from left to right) the $S_{21}(0)$ ↑, $R_{22}(4)$ ↑, $R_{22}(6)$ ↑, $R_{22}(8)$ ↑ and $S_{21}(12)$ ↑ transitions populating the f_2 spin-rotational level of NO(A). The error bars were determined using a Monte Carlo procedure [60], and represent 95% confidence limits. The experimental data are compared with the results of the simulations based on the 'open shell' QCT depolarization cross-section data, $\sigma_N^{(2)}/\text{Å}^2$, which are also presented.

N'	2	5	7	9	14
Hyperfine	40.9 ± 11.6	13.2 ± 3.2			
Zeeman		18.9 ± 3.7	12.0 ± 3.2	9.5 ± 3.1	6.5 ± 4.4
QCT total	44.0	16.4	9.6	5.5	1.0
QCT elastic	7.2	2.5	1.4	0.8	0.4
QCT inelastic	36.8	13.9	8.2	4.7	0.6

TABLE III: As for Table II, but showing the thermal (300 K) depolarization cross-sections for 'disalignment' ($\sigma_3^{(2)}/\text{Å}^2$) of NO(A) by He. The experimental data are compared with the results of the 'open shell' QCT depolarization cross-section data, $\sigma_N^{(2)}/\text{Å}^2$.

N'	2	5	7	9	14
Zeeman	50 ± 9	45 ± 7	33 ± 8	36 ± 10	18 ± 4
Simulation	83	60			13
QCT total	81.0	54.1	34.3	20.5	4.9
QCT elastic	4.8	3.1	2.7	2.1	1.7
QCT inelastic	76.2	51.0	31.6	18.4	3.2

TABLE IV: As for Table II, but showing the thermal (300 K) depolarization cross-sections for 'disorientation', $\sigma_3^{(1)}/\text{Å}^2$, of NO(A) by Ar. The experimental data are compared with the results of the simulations based on the 'open shell' QCT depolarization cross-section data, $\sigma_N^{(1)}/\text{Å}^2$, which are also presented.

N'	2	5	7	9	14
Zeeman	20.8 ± 3.3	15.4 ± 3.3	9.1 ± 1.9	10.5 ± 2.7	5.6 ± 1.3
QCT total	29.4	10.8	6.1	3.0	0.4
QCT elastic	3.4	1.0	0.5	0.3	0.2
QCT inelastic	26.0	9.8	5.6	2.7	0.2

TABLE V: As for Table II, but showing the thermal (300 K) depolarization cross-sections for 'disorientation', $\sigma_3^{(1)}/\text{Å}^2$, of NO(A) by He. The experimental data are compared with the results of the 'open shell' QCT depolarization cross-section data, $\sigma_N^{(1)}/\text{Å}^2$.

FIG. 1: (Colour online.) Top panel: An example of a Zeeman beat signal for NO(A) $f_2, v = 0, N = 14$ (dashed line, black), together with a fit to the data (continuous line, red), obtained at a magnetic field strength of around 20 Gauss. The signal was obtained with $\leq$0.5 mTorr of NO and no quencher gas present, and probes the angular momentum alignment of NO(A). Bottom panel: Comparison of the experimental relative beat intensity, obtained from the decay shown in the top panel by subtracting of the appropriate exponential decay, with the calculated relative intensity based on (1+1) LIF linestrength theory [59].

FIG. 2: (Colour online.) Top panel: As for the top panel of Fig. 1, but showing the hyperfine beat signal for NO(A) $f_2, v = 0, N = 2$ in the absence of an applied magnetic field. The signal was obtained with $\leq$0.5 mTorr of NO without quencher gas present, and probes the angular momentum alignment of NO(A). The experimental data is the black dashed line, and the simulation is shown as the continuous red line. Bottom panel: Comparison of the experimental relative beat intensity, obtained from the decay shown in the top panel by subtracting of the appropriate exponential decay, with the calculated relative intensity based on (1+1) LIF linestrength theory [59] and Eq. (21) [61] (continuous line, red).

FIG. 3: (Colour online.) Left panels: Comparison of the c–s QM and (closed shell) QCT fixed energy (39 meV) and thermally averaged rotational energy transfer (top), disorientation (middle), and 'disalignment' (bottom) cross-sections for NO(A) + Ar in the initial state $N = 2$ and resolved in N'. Right panels: total inelastic (top), disorientation (middle), and 'disalignment' (bottom) cross-sections resolved in N, but summed over N'.

FIG. 4: (Colour online.) Comparison of the 'open shell' QCT rotational energy transfer (top panels), disorientation (middle panels), and disalignment (bottom panels) cross-sections obtained using the tensor opacity formalism of ref. [15] with the full open shell QM calculations. The data are for the initial state $N = 2, j = 1.5$, and are resolved in N'. Cross-sections for spin-rotation conserving (labelled SC) transitions are shown on the left, while those for the spin-rotation changing (NSC) collisions are shown on the right.

FIG. 5: (Colour online.) Effect of quencher gas pressure on the LIF signal (left) and the relative hyperfine beat intensity (right) for NO(A) $f_1, v = 0, N = 2$. Measurements were conducted with 0.5 mTorr of NO, and 0 mTorr (top panels), 200 mTorr (middle panels), and 400 mTorr (bottom panels) of He quencher gas, and are sensitive to the angular momentum alignment.

FIG. 6: (Colour online.) As for Fig. 5, but showing the effect of quencher gas pressure on the Zeeman beat relative intensity. The data were obtained using circularly polarized laser radiation, and probe the angular moment orientation. The data are for NO(A) $f_2, v' = 0, N' = 9$ with Ar, and were obtained at a field of 10 Gauss.

FIG. 7: (Colour online.) Disorientation and 'disalignment' thermally averaged depolarization cross-sections for NO(A) by Ar (red/light gray circles) and He (blue/dark gray triangles). Solid lines/points are from Zeeman quantum beat fluorescence decays, dotted lines/open points are from hyperfine decays.

FIG. 8: (Colour online.) Experimental thermally averaged (300 K) rotational energy transfer [67–69] (top panel), disorientation (middle panel), and 'disalignment' (bottom panel) cross-sections for NO(A) + Ar. Also shown are the results of the 'open shell' fixed energy (39 meV) QCT calculations (open squares). The experimental data in the top panel, shown as filled triangles, are taken from refs. [67–69].

FIG. 9: (Colour online.) As for Fig. 8, but showing the rotational energy transfer and depolarization cross-sections for NO(A) by He. Experimental rotational energy transfer data, shown as filled triangles in the top panel, are taken from Refs. [67, 68].

FIG. 10: (Colour online.) Schematic energy level diagram for NO(A). The ordering of the levels is consistent with that shown in refs. [62, 78]. Note the change in the ordering of both the Zeeman levels and the hyperfine levels for the two spin-rotation states of NO($A^2\Sigma^+$) shown.

FIG. 11: (Colour online.) Comparison between the experimental disorientation (left panel) and 'disalignment' (right panel) thermally averaged cross-sections for NO(A) + Ar and those obtained from the simulations using the 'open shell' QCT data. Unlike the QCT data shown in Fig. 8, the simulations take full account of the dephasing effects discussed in the text.

FIG. 12: (Colour online.) Comparison of QCT RET cross-sections (top panel), alignment depolarization moments (middle panel), and 'disalignment' cross-sections (bottom panel) from $N = 7$ resolved in N', showing the effect of the potential energy surface versus kinematics.

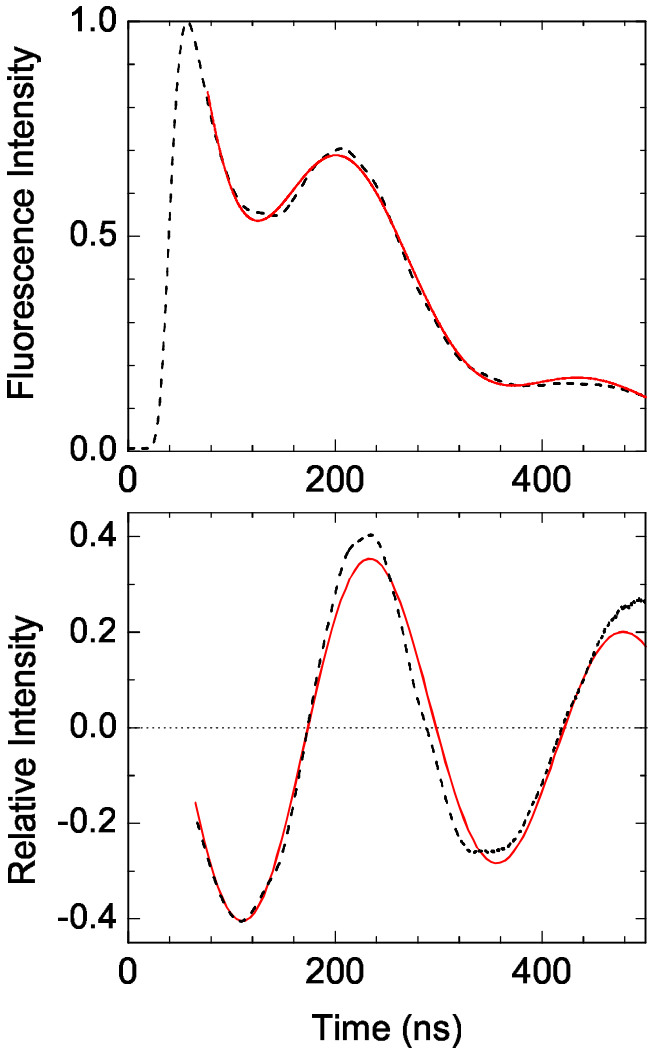

Brouard *et al.* Figure 1

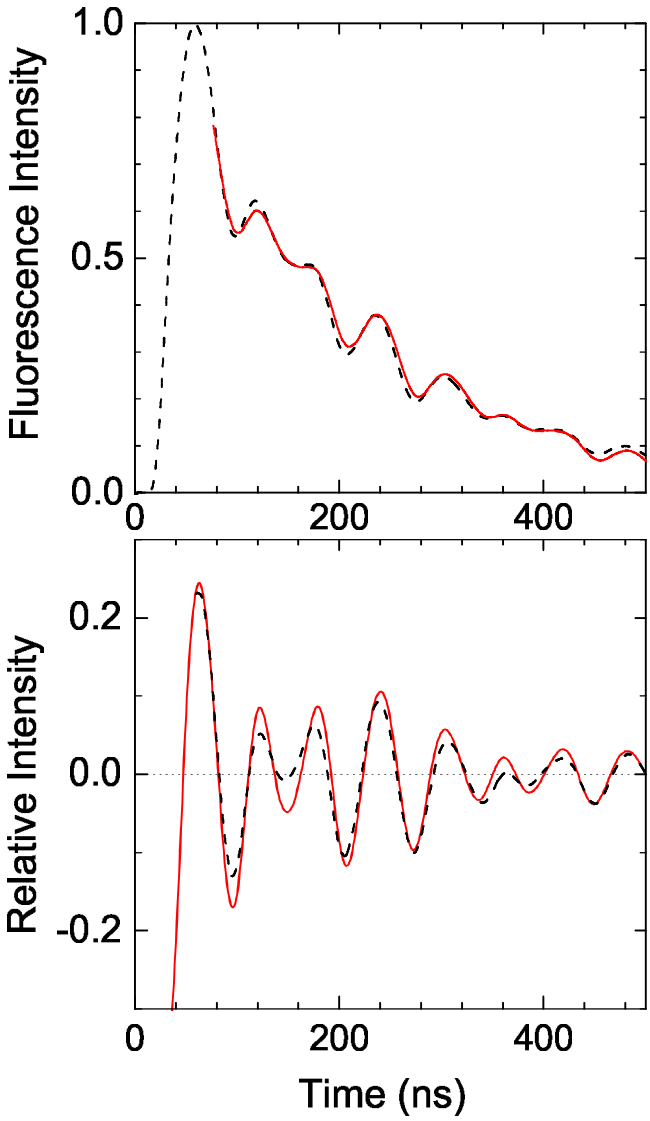

Brouard *et al.* Figure 2

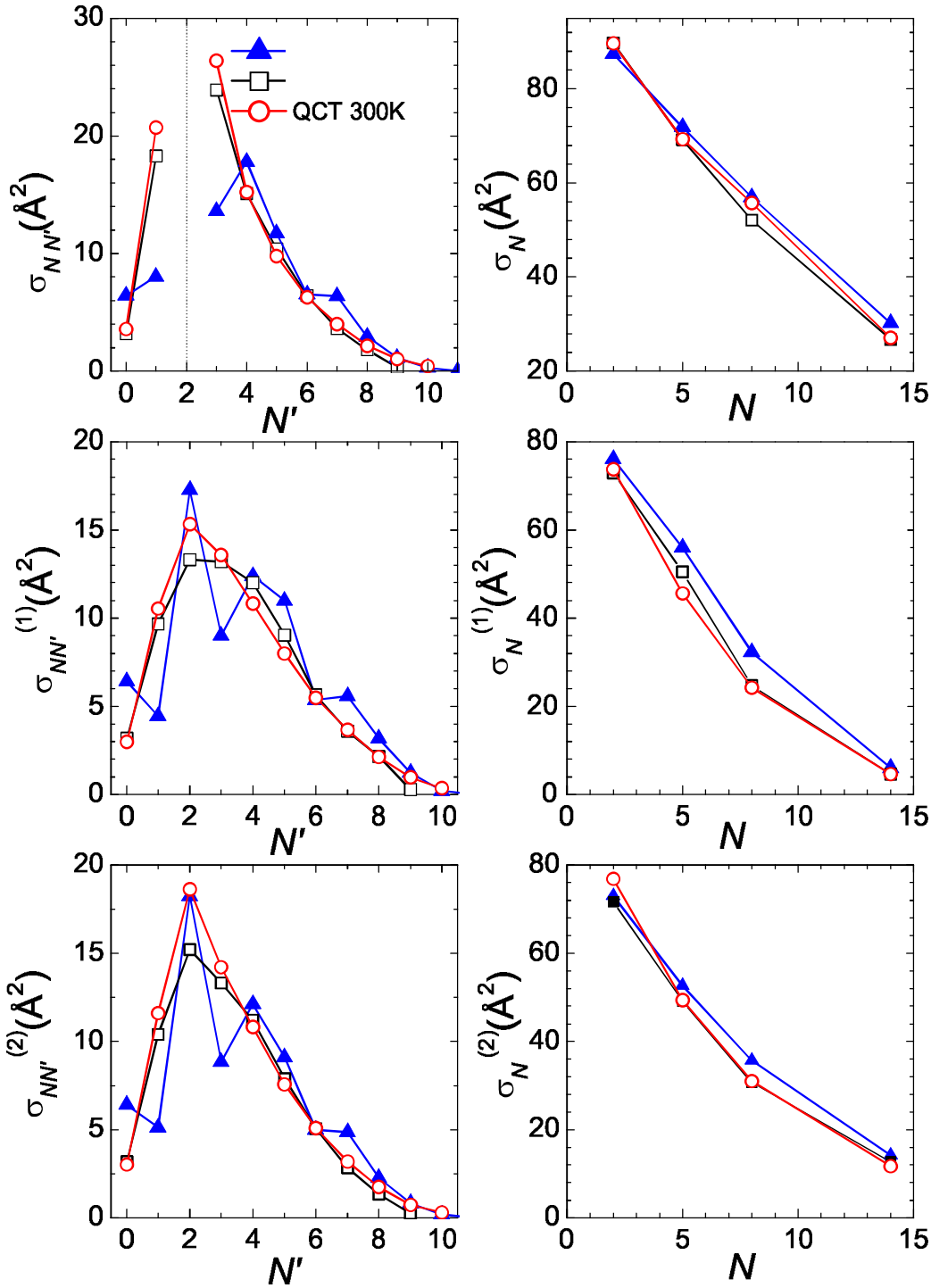

Brouard *et al.* Figure 3

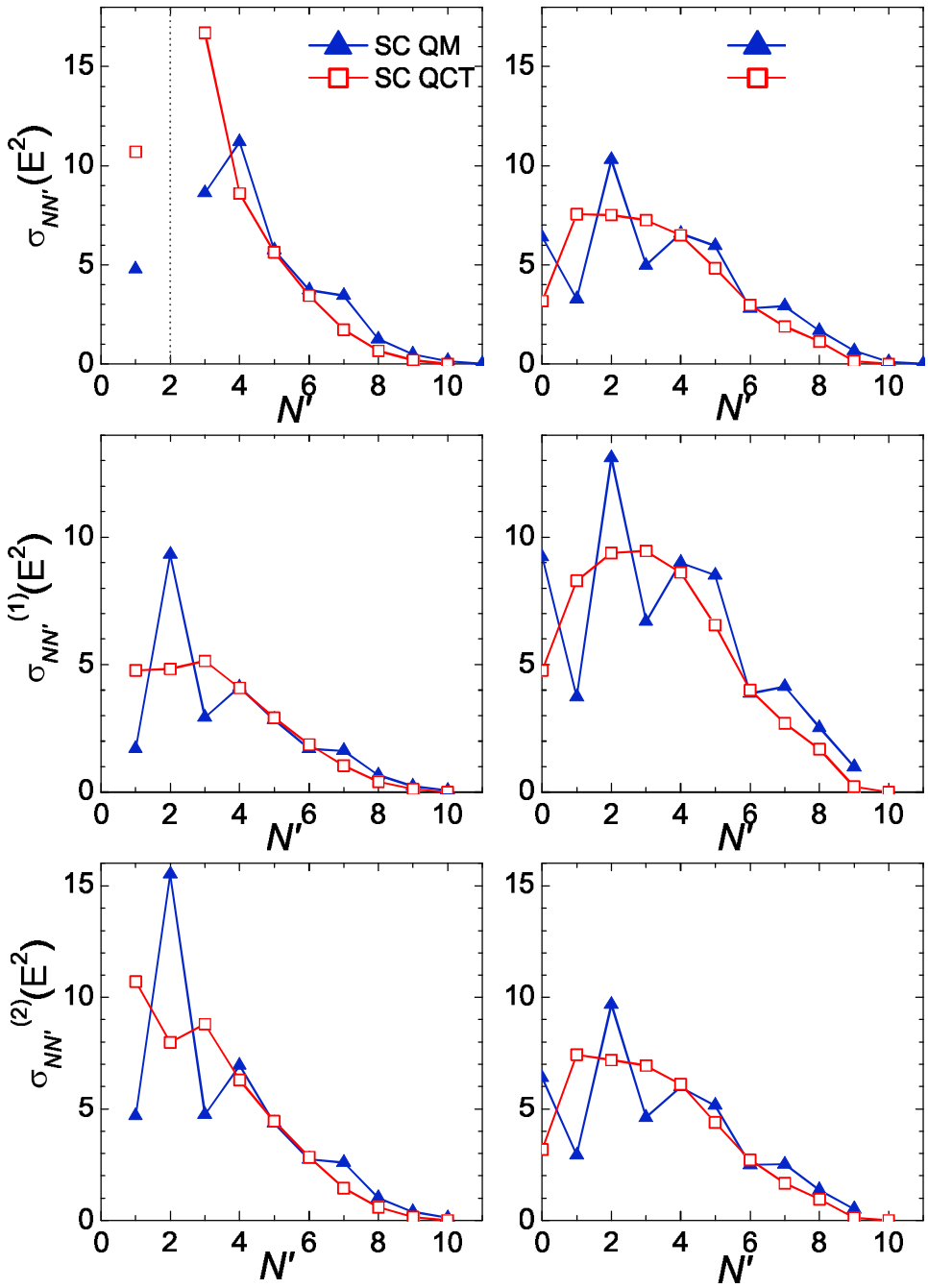

Brouard *et al.* Figure 4

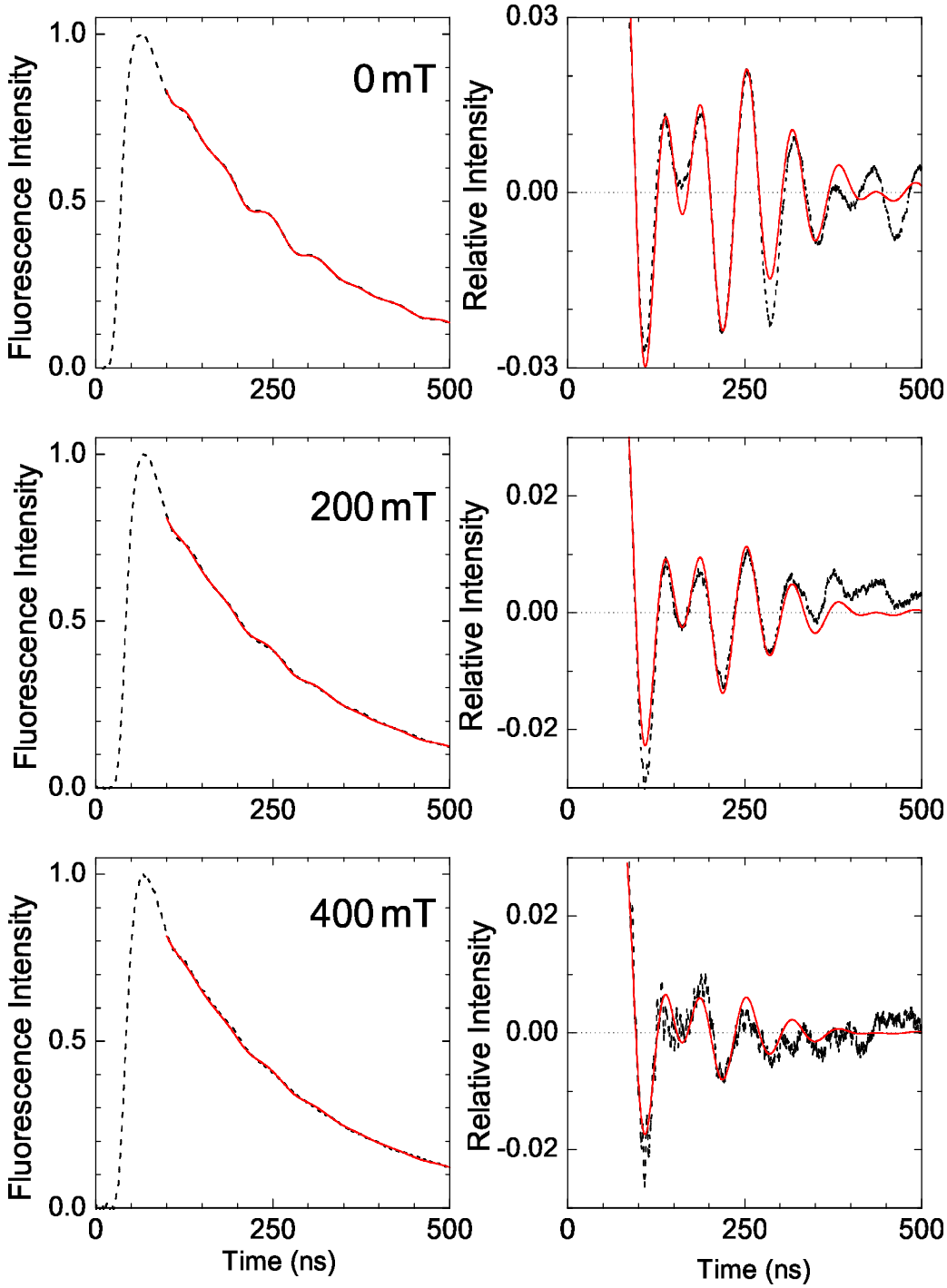

Brouard *et al.* Figure 5

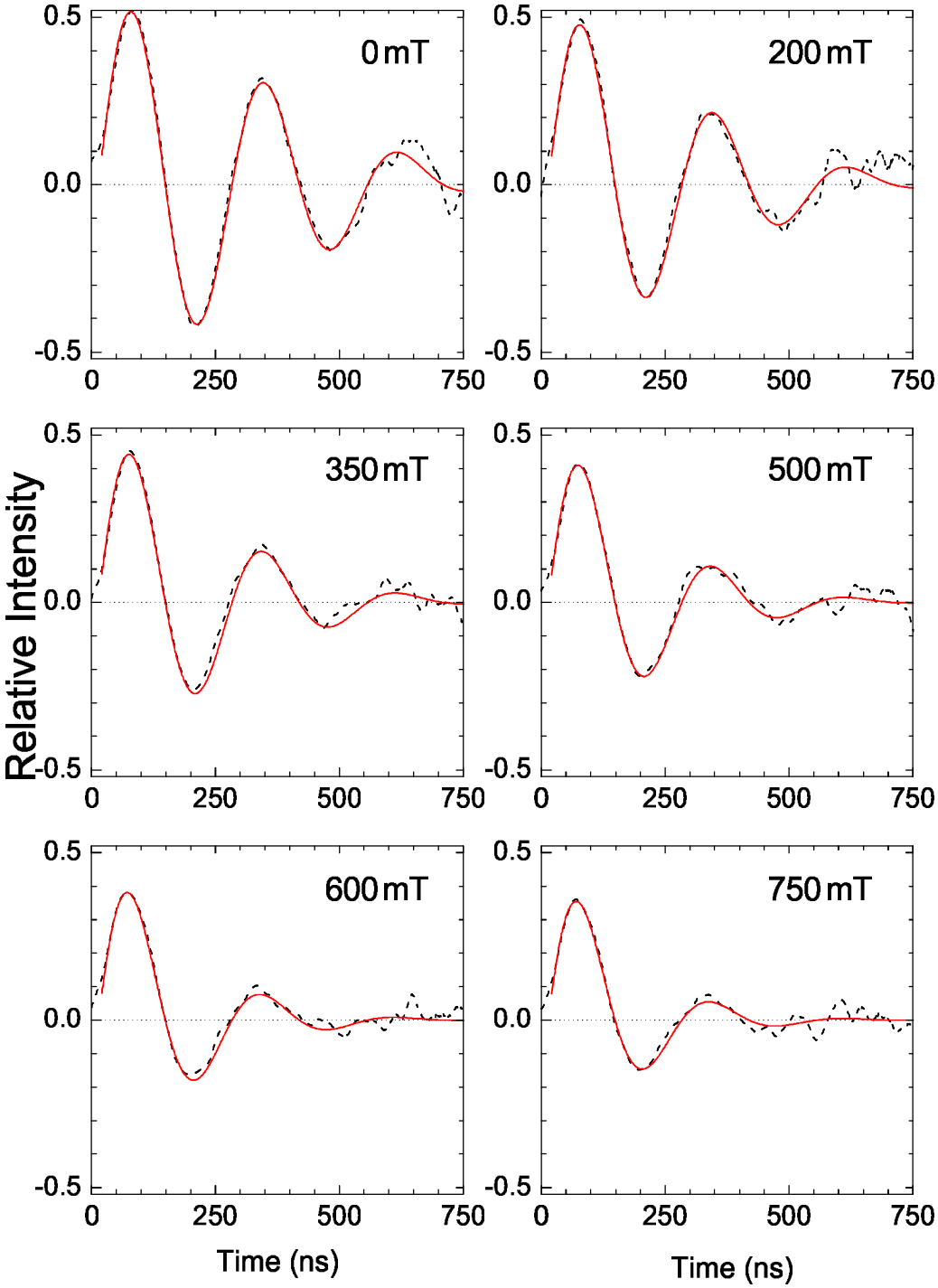

Brouard *et al.* Figure 6

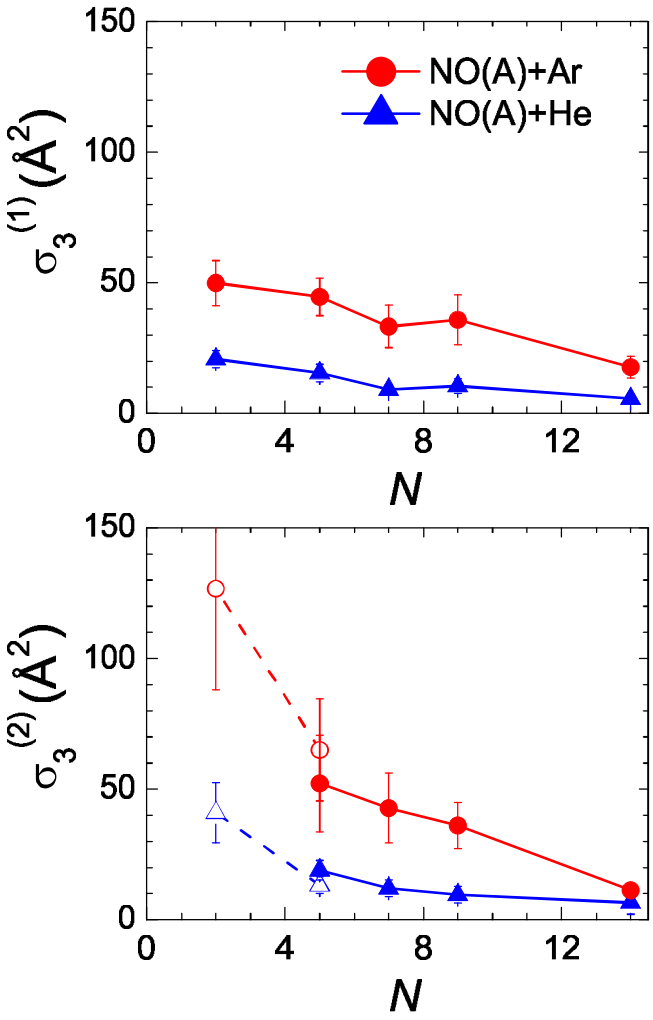

Brouard *et al.* Figure 7

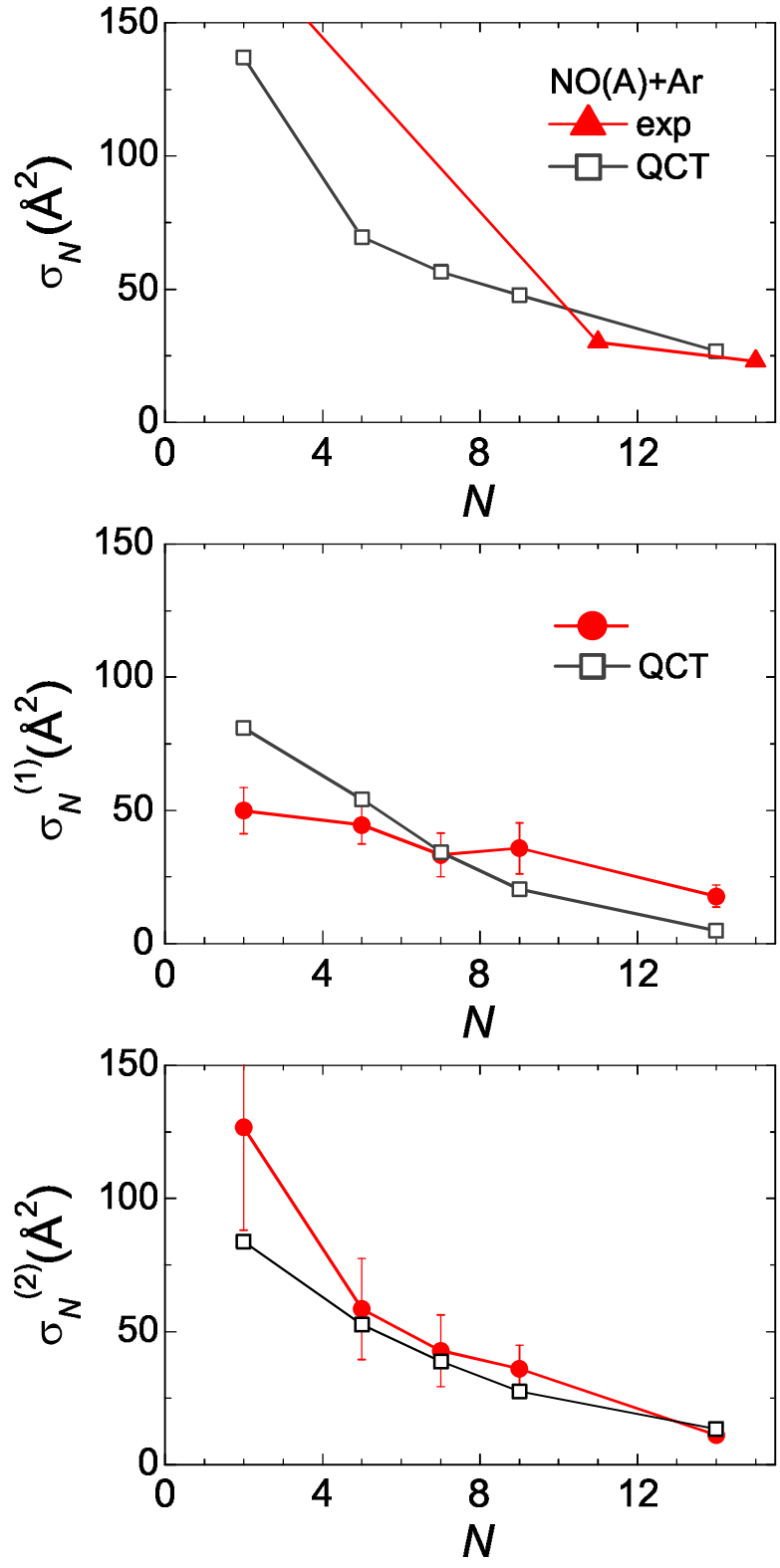

Brouard *et al.* Figure 8

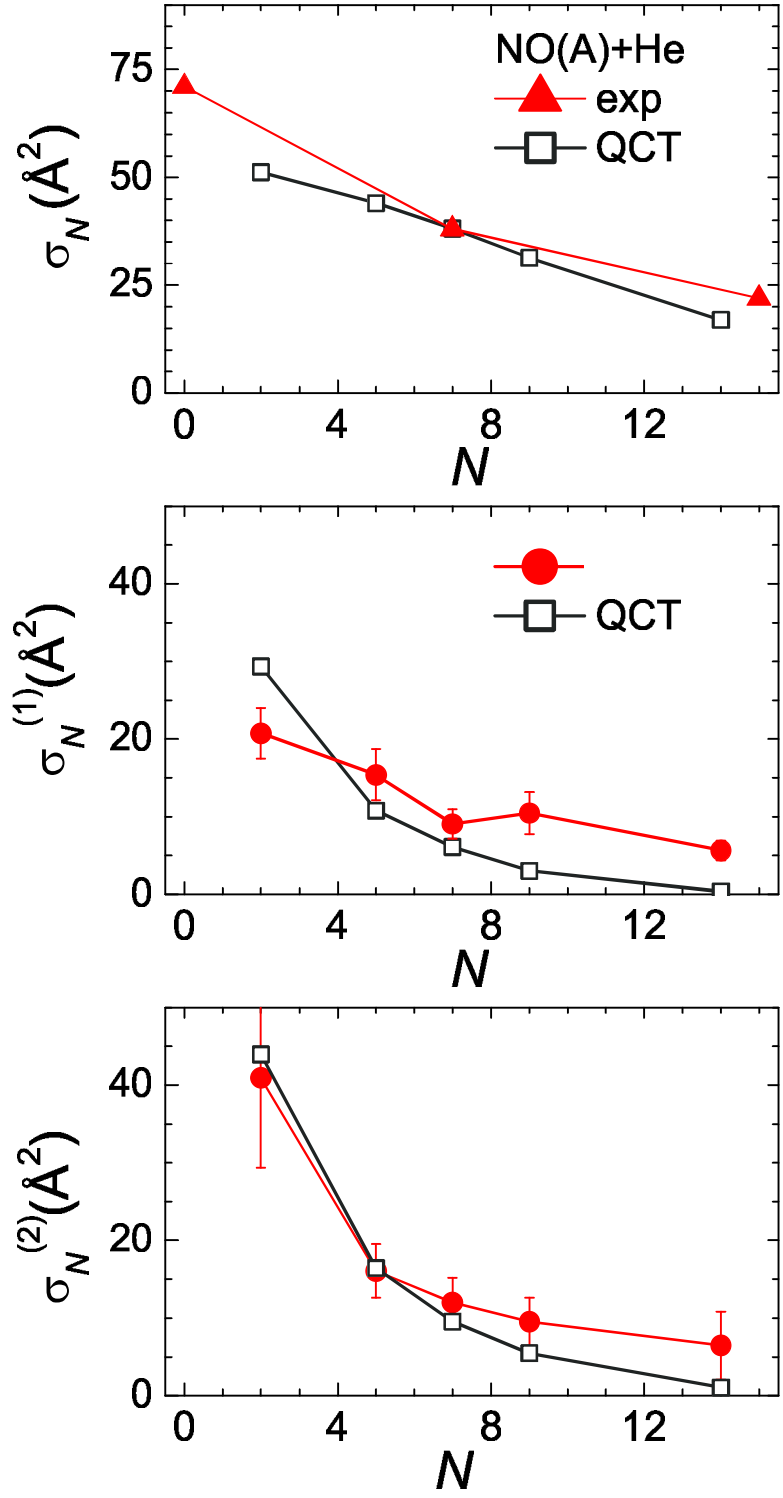

Brouard *et al.* Figure 9

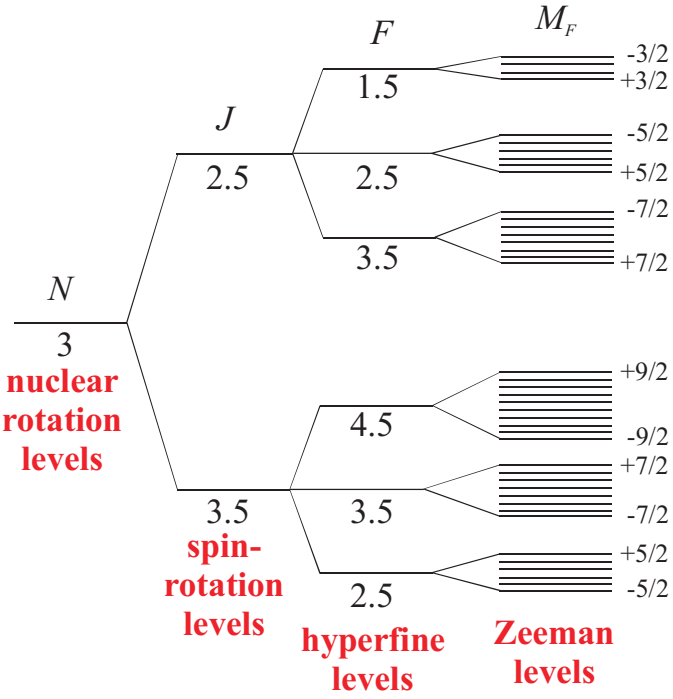

Brouard *et al.* Figure 10

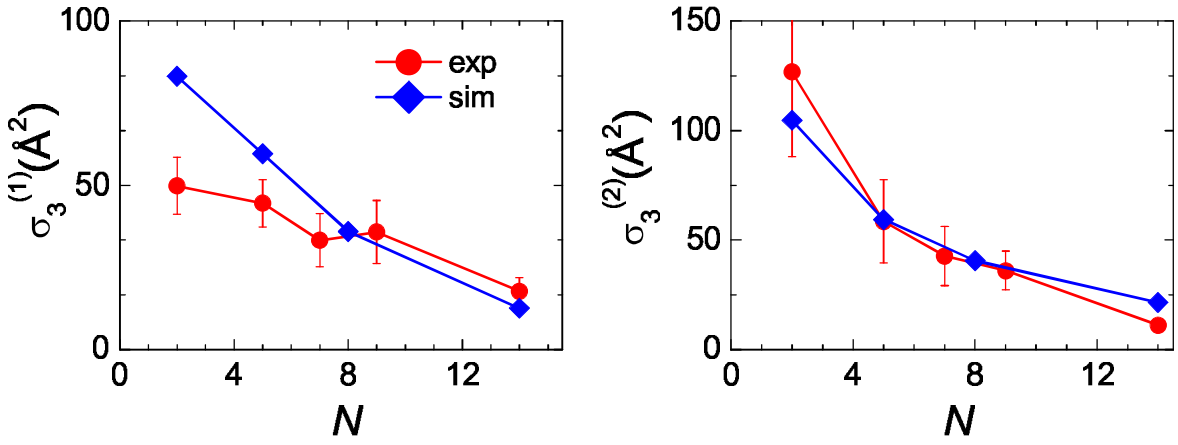

Brouard *et al.* Figure 11

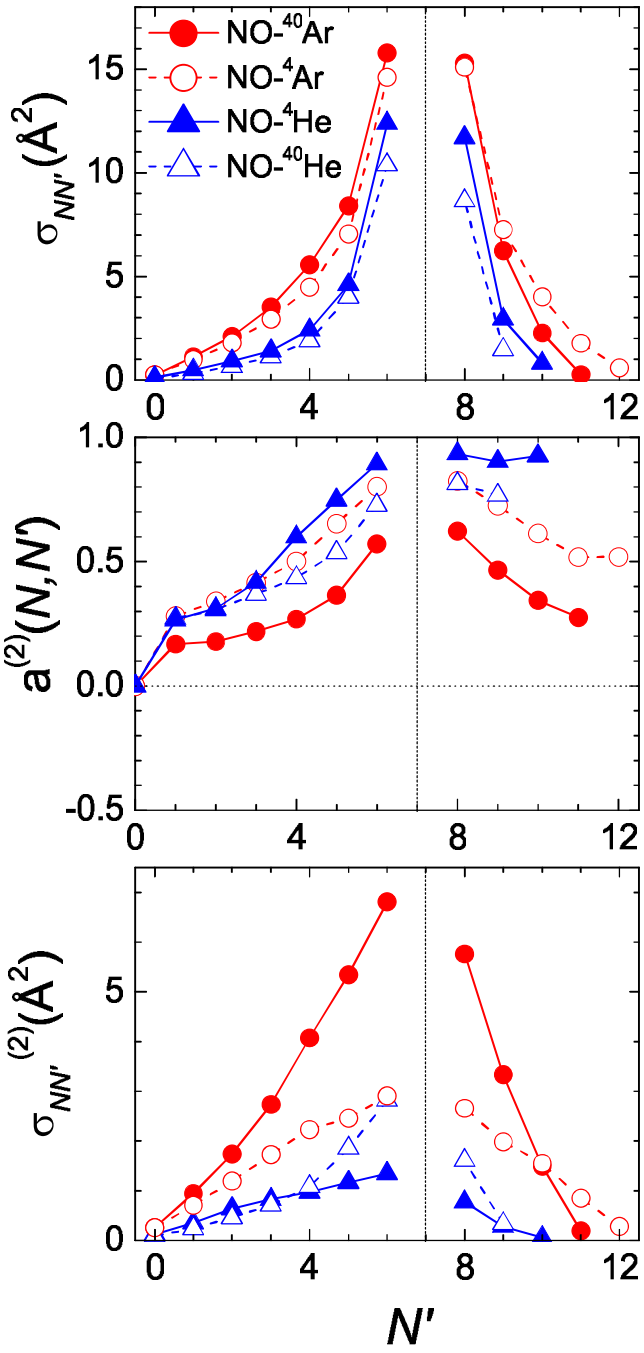

Brouard *et al.* Figure 12